

Inverse Modeling the Brazil-Malvinas Confluence

Dorleta Orúe-Echevarría¹ , Josep L. Pelegrí¹ , Francisco Machín²,
Alonso Hernández-Guerra³ , and Mikhail Emelianov¹

¹Department d'Oceanografia Física i Tecnològica, Institut de Ciències del Mar, Consejo Superior de Investigaciones Científicas, Unidad Asociada ULPGC-CSIC, Barcelona, Spain, ²Departamento de Física, Universidad de Las Palmas de Gran Canaria, Las Palmas de Gran Canaria, Spain, ³Instituto de Oceanografía y Cambio Global, Universidad de Las Palmas de Gran Canaria, Unidad Asociada ULPGC-CSIC, Las Palmas de Gran Canaria, Spain

Key Points:

- We apply an inverse model to determine barotropic, baroclinic, and total volume transports at two different spatial scales encircling the Brazil-Malvinas Confluence
- Both cruise and model data show a weak along-slope Malvinas Current at 41°S (28 Sv) and a much more intense northward interior branch (79 Sv) into the confluence
- The confluence holds substantial cross-frontal exchange, including the subduction of subantarctic layers and their diapycnal mixing with subtropical waters

Supporting Information:

- Supporting Information S1

Correspondence to:

D. Orúe-Echevarría and J. L. Pelegrí,
dorleta.orue@gmail.com;
pelegrí@icm.csic.es

Citation:

Orúe-Echevarría, D., Pelegrí, J. L., Machín, F., Hernández-Guerra, A., & Emelianov, M. (2019). Inverse modeling the Brazil-Malvinas Confluence. *Journal of Geophysical Research: Oceans*, 124, 527–554. <https://doi.org/10.1029/2018JC014733>

Received 2 NOV 2018

Accepted 2 JAN 2019

Accepted article online 5 JAN 2019

Published online 21 JAN 2019

Abstract The Brazil-Malvinas Confluence arises from the frontal encountering of the subtropical Brazil Current and subantarctic Malvinas Current. It displays a complex regional circulation that is accompanied by mesoscale features and thermohaline intrusions. Here we combine altimetry and cruise data to describe the circulation pattern in the upper 2,000 m at two spatial scales encircling the frontal system. The major regional features appear south of the confluence latitude at 39–40°S: (a) a relatively weak Malvinas Current near 41°S, 56°W (28.3 ± 1.4 Sv), followed by its cyclonic retroflection; (b) an intense subtropical anticyclone (59.3 ± 10.7 Sv) that replaces the Brazil Current overshoot; and (c) a very intense subantarctic inflow (78.9 ± 13.7 Sv) near 53°W that is maintained through both an upstream (near 42°S) earlier diversion of the Malvinas Current and the cyclonic recirculation of the flow exiting east along the confluence. North of the confluence, the Brazil Current provides a net input of 30.8 ± 12.0 Sv (29.1 ± 8.3 Sv along the slope). The southern inflow splits nearly equal between barotropic and baroclinic contributions while the entire northern flow is essentially baroclinic. These northern and southern inputs add to an eastward along-front transport of 109.7 ± 15.1 Sv, with significant contribution of highly oxygenated, relatively fresh Subantarctic Mode and Antarctic Intermediate Waters (58.7 ± 5.6 Sv). The regional circulation experiences substantial temporal variability, with southern waters flowing into the Brazil-Malvinas Confluence through along-slope and interior pathways and partly recirculating within the subtropical South Atlantic gyre.

Plain Language Summary The Brazil Malvinas Confluence is an intense frontal system, the meeting point of the southward Brazil Current, which transports subtropical relatively warm, salty, and poorly oxygenated waters, and the Malvinas Current, carrying subantarctic relatively fresh, cold, and highly oxygenated waters. Here we examine the conditions in the confluence at the time of the TIC-MOC cruise, paying special attention to their previous evolution. South of the confluence (39–40°S), the circulation is characterized by a relatively weak along-slope Malvinas Current and an interior intense dipole while north of the confluence the main current is the along-slope Brazil Current; the southern and northern inputs conduce to a very intense eastward along-front South Atlantic Current. We find that the conditions at the confluence are forced by both the impinging boundary currents and the interior ocean conditions. Further, the confluence is a site where subantarctic waters flow underneath the subtropical layers and recirculate south after experiencing substantial transformations in the subtropical gyre. We may conclude that the confluence acts both as a barrier and a blender of subtropical and subantarctic waters, of especial relevance in the meridional transport of heat and other properties.

1. Introduction

An outstanding regional feature in the world ocean is the collision of the Brazil and Malvinas Currents (BC and MC), two major western boundary currents that carry waters of subtropical and subantarctic origin. The outcome of this encounter is a very intense thermohaline frontal system, the Brazil-Malvinas Confluence (BMC), with possibly the highest temperature horizontal gradients in the open ocean. The characteristics of the BMC, as for any frontal system, will depend on the relative effect of the advective and diffusive processes: the intensity of the impinging currents, as the element that brings together waters with contrasting characteristics, and the cross-frontal exchange, as the process that tends to dilute the differences in water properties.

Current descriptions of the BMC circulation pattern rely on remote sea surface temperature (SST) and altimetry data, hydrography and velocity data from shelf and slope moorings, and relatively low-resolution hydrographic data from regional cruises. The BMC mean position is about 38°S, with a seasonal cycle of nearly 3° along the continental shelf break, reaching its northernmost position during austral winter (Goni et al., 2011; Goni & Wainer, 2001; Gordon & Greengrove, 1986; Saraceno et al., 2004). The MC runs north along the Argentinean slope until the BMC, where it sharply turns south as the Malvinas Return Current (MRC) (Piola et al., 2013) before finally flowing east at about 45°S (Peterson & Whitworth, 1989). The BC also follows close to the slope until the BMC, where it separates from the continent and continues at the eastern side of the MRC, drawing a loop known as the Brazil Current Overshoot (BCO) (Saraceno et al., 2004). Parts of the MRC and BCO continue eastward at about 40°S as the South Atlantic Current (SAC) while other portions recirculate north to feed back the latitudinal flows into the BMC (Stramma & Peterson, 1990).

Several studies have analyzed the mean intensity and variability of the MC and BC. Early estimates of the MC—assuming that the current is in geostrophic balance—ranged between 5 and 15 Sv ($1\text{ Sv} = 10^6\text{ m}^3/\text{s} \cong 10^9\text{ kg/s}$) (Garzoli, 1993; Gordon & Greengrove, 1986). However, these estimates did not consider a substantial barotropic contribution. Studies that combine hydrographic or altimetry data with direct current measurements have indeed reported higher transports, in the 35–60-Sv range (Peterson, 1992; Saunders & King, 1995; Spadone & Provost, 2009; Vivier & Provost, 1999a). Artana et al. (2018) combined 25 years of altimetry and mooring data to obtain a transport of 37.1 ± 6.6 Sv, with several instances of transports greater than 50 Sv. In contrast, most of the mean BC transport is baroclinic (Matano et al., 2010), so different geostrophic calculations have provided more consistent numbers. The BC volume transport generally increases with latitude, as a consequence of water recirculation within the subtropical gyre: 10 Sv at 24°S (Stramma, 1989), 20–30 Sv at 32°S (Garzoli et al., 2013; Schmid, 2014; Zemba, 1991), and 20–40 Sv at 38°S, close to the BMC (Garzoli, 1993; Garzoli & Garraffo, 1989; Gordon & Greengrove, 1986; Maamaatuaiahutapu et al., 1998; Piola & Matano, 2001).

Contrasting with the above extensive descriptions of the MC and BC, there are fewer studies on why and how the BMC frontal system becomes unstable and, particularly, on how this instability leads to cross-frontal exchange. At the locus of the collision, the BMC generally appears as one single frontal system, commonly named BMC front; on the leeside of the encounter, however, there are two well-differentiated fronts: the Subantarctic Front (SAF), as the northernmost front associated to the Antarctic Circumpolar Current (Artana et al., 2016; Orsi et al., 1995), and the Brazil Current Front (BCF), which sets the southern limit of the BC (Peterson & Whitworth, 1989). The latitude and longitude of these fronts changes continuously in time, at scales that vary from weeks to years. Several recent studies have identified the existence of two opposite regimes in the BMC—named weak and strong Malvinas flow—which are expressed in terms of the intensity of the along-slope MC near 41°S (Artana et al., 2018; Ferrari et al., 2017; Paniagua et al., 2018). During the weak Malvinas regime, the SAF does not reach 41°S over the slope, the BCF overshoots as far as 44°S, and the eddy kinetic energy (calculated at time scales less than 20 days) increases; during the strong Malvinas regime, the SAF and BCF meet near 39°S along the slope, the BCO breaks down as an isolated anticyclone, and the eddy kinetic energy decreases. Despite this useful idealization, the time series of sea-surface altimetry show that the actual state at any time is quite complex (Ferrari et al., 2017), some sort of combination of both longitudinal and latitudinal dipoles (and even tripoles) that results in a highly variable and difficult to interpret pattern of mesoscale and regional recirculations.

Our lack of understanding of the processes that control the patterns of regional circulation becomes even more evident when we attempt to describe those processes that lead to net exchange across the frontal system. These include the latitudinal motions of a myriad of mesoscale features of both signs (Legeckis & Gordon, 1982; Olson et al., 1988; Lentini et al., 2006; Saraceno & Provost, 2012; Mason et al., 2017), and the subduction and thermohaline intrusions of subantarctic and subtropical mode waters (Gordon, 1981; Provost et al., 1999; Sato & Polito, 2014). This is relevant both regionally and globally, as the outcome of the horizontal and vertical processes at the BMC is a substantial transformation of those water masses that will ultimately flow to the North Atlantic Ocean as the returning limb of the Meridional Overturning Circulation (MOC) (Garzoli & Matano, 2011).

The purpose of this study is to produce a detailed portrait of the frontal structure and associated surface and subsurface circulation patterns in a relatively small region encompassing the BMC (Figure 1), placing this

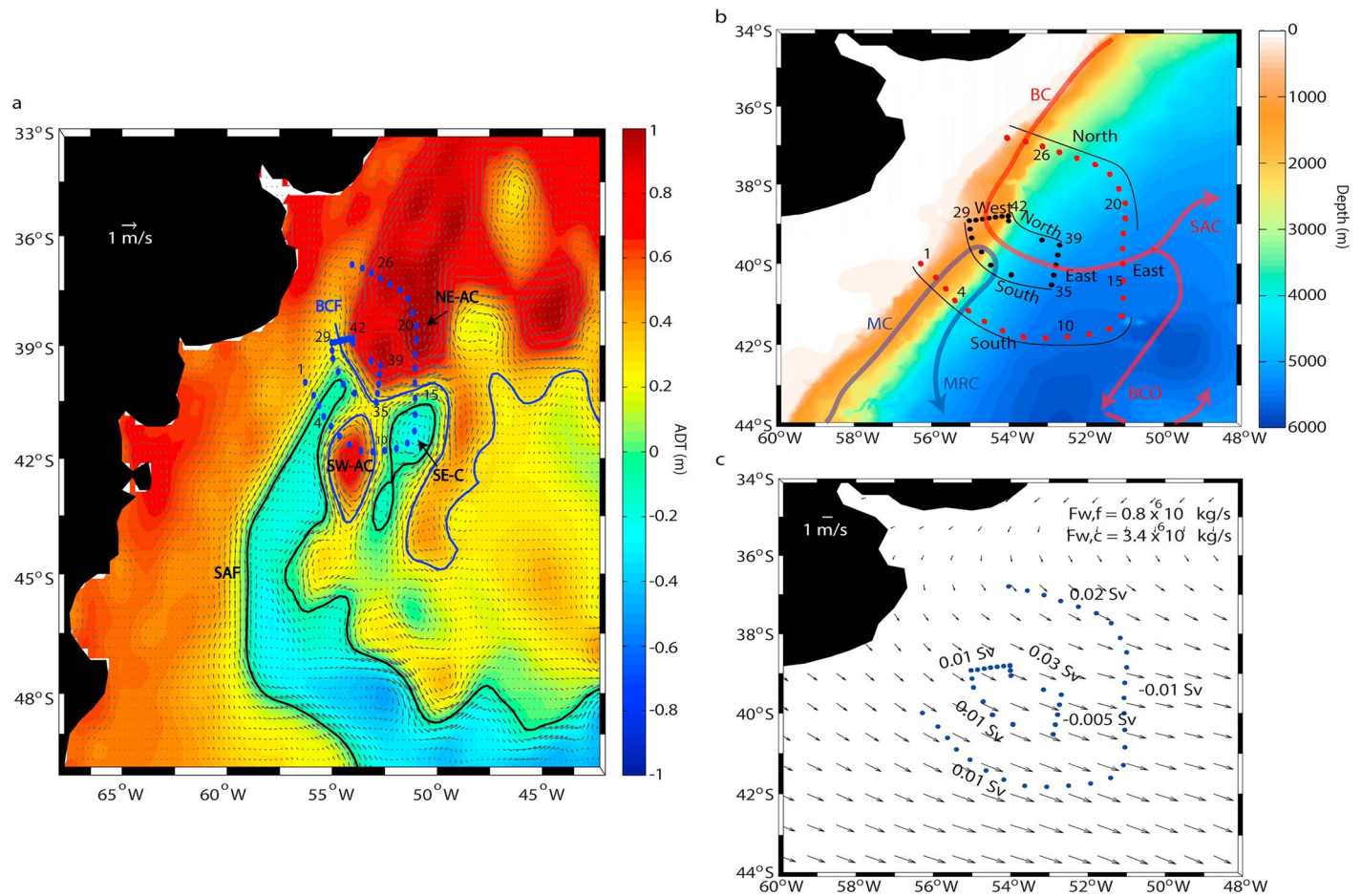


Figure 1. (a) Mean sea-surface ADT (m) in the South-Western Atlantic Ocean for March 2015 and mean surface geostrophic velocities (black arrows) together with the location of the Brazil Current Front (BCF; blue line) and the Subantarctic Front (SAF; black line), ADT values for each of the fronts as in Ferrari et al. (2017). The positions of the hydrographic stations are shown as blue dots. (b) Location of the hydrographic stations on top of the bathymetry (GEBCO 2008; color-coded, in m), distinguishing those stations used for the confluence (red dots, stations 1–28) and frontal (black dots, stations 29–47) models; the north, south, east, and west positions of each perimeter are shown for reference. The predominant paths of the BC and MC, at the time of the cruise, are sketched. (c) Mean March 2015 sea-surface winds in the study area; the sea-surface Ekman transports (Sv) through each portion of the perimeter are indicated, with positive values denoting transfer out of the domain. The net freshwater fluxes for the frontal ($F_{w,f}$) and confluence ($F_{w,c}$) domains are shown in the top right, with positive values denoting net transfer toward the ocean.

snapshot in perspective with the frontal evolution at time scales of months. We aim at describing the specific state at the time of the cruise, not only identifying the associated circulation patterns but also exploring what their complexity tells us about the frontal evolution and dominant processes. For this purpose, we combine high-resolution hydrographic and velocity data in the upper 2,000 m, from a cruise carried out in March 2015, with velocity time series for the along-slope MC at about 41°S (Ferrari et al., 2017; Saraceno et al., 2017; Paniagua et al., 2018) and remote-sensing altimetry and temperature data over the entire region. The baroclinic and barotropic water mass transports are calculated using inverse models at two different spatial scales: frontal area and confluence region. The frontal area focuses on the flow at the frontal system itself while the confluence region is used to describe the characteristics of the impinging BC and MC, as well as the MRC and BCO.

The structure of the article is as follows. The cruise and remote sensing data are introduced in section 2, and the fundamentals and application of the inverse model are presented in section 3. Section 4 shows the surface geostrophic velocity fields and the hydrographic properties along the frontal and confluence perimeters, and section 5 presents the velocities and transports into or out of the frontal and confluence domains as deduced with the inverse model. In section 6 we compare the velocity fields as sampled with the ship and calculated with the inverse model, provide our best estimate of the transports associated with

the main flow patterns, and assess the water transformations at the frontal system. We conclude in section 7 with some remarks about what we have learnt and what yet remains unknown regarding the mean flow structure in the BMC.

2. Data

2.1. TIC-MOC Cruise

The TIC-MOC cruise was carried out onboard the R/V *Hespérides* between 8 and 22 March 2015 (Figure 1). The positioning of the hydrographic stations relative to the BMC was done using near real-time remote sensing altimetry and temperature data (see next section), as well as one-week-window daily forecasts of sea-surface absolute dynamic topography (ADT) and temperature, salinity, and velocity at 0, 92, 453, and 1062 m, as provided by the Mercator Ocean PSY4QV2R2 operational model, with $1/12^\circ$ resolution (<https://www.mercator-ocean.fr/>). A full description of the cruise methods and sampling is presented by Orúe-Echevarría et al. (2019) and the entire data set is available at Pelegrí et al. (2018), a summary follows.

A total of 66 hydrographic stations were done in the BMC, with 19 stations bounding the inner part of the front (frontal area) and 28 stations delimiting a larger and more external domain (confluence region) (Figure 1). Conductivity-temperature-depth (CTD) data were obtained with a SeaBird 911 Plus multiparametric probe, with duplicate salinity and temperature sensors in order to detect any possible drift, and dissolved oxygen (DO) was sampled with a SBE-43 sensor and calibrated through Winkler titration of a selected number of samples.

The frontal area is aligned with the frontal system, with a near-rectangular shape approximately $250 \text{ km} \times 100 \text{ km}$. The mean distance between stations is 30 km, although it varies from 15 km in the western section to 90 km between the two most-spaced northern stations; the frontal stations reached down to either the seafloor over the upper slope or 400 m in the open ocean. The confluence stations follow a nearly circular perimeter, with diameter about 500 km, closed to the west by the continental slope. These stations stretched down to the seafloor over the upper slope or a minimum depth of 2,000 m in the open ocean, with the distance between each pair of stations close to 45 km everywhere. For all stations, conservative temperature (θ), absolute salinity (S), and neutral density (γ^n) are calculated with 2-dbar vertical resolution.

Horizontal velocity profiles were obtained at each hydrographic station through a lowered acoustic Doppler current profiler (LADCP). Due to the flooding of the upper-looking LADCP, in most stations the velocity was recorded using only the 300-kHz downward looking LADCP, for 4-m vertical bins. Additionally, throughout the cruise, the vessel-mounted ADCP (VADCP) continuously sampled the horizontal currents between about 20 and 700 m, using 8-m depth bins.

2.2. Supplementary Data Sets

We use remote-sensing altimetry data in order to obtain surface velocities and locate the surface fronts. The daily ADT and corresponding surface geostrophic velocities come from the DUACS multisatellite $1/4^\circ$ gridded delay-time product (Pujol et al., 2016), as provided by the Copernicus Marine Environment monitoring service (<http://marine.copernicus.eu/>). The mean March 2015 ADT field characterizes the surface flow at the time of the cruise and delimits the position of the SAF and BCF using the ADT definitions in Barré et al. (2011) and Ferrari et al. (2017)—contours of $+0.30 \text{ m}$ for the BCF and -0.05 m for the SAF. We also use level-3 SST images from the Advanced Very High Resolution Radiometer on National Oceanic and Atmospheric Administration satellites, with a spatial resolution of 4 km (<https://data.nodc.noaa.gov>).

We obtain sea-surface wind stress and evaporation-precipitation ($E-P$) data (spatial resolution $0.75^\circ \times 0.75^\circ$) from the European Centre for Medium-Range Weather Forecasts (<https://www.ecmwf.int/>). From the wind stress we calculate the Ekman transports T_E into or out of either the frontal or confluence domains; similarly, from the $E-P$ values we compute the freshwater transports F_w for either dominion (Figure 1c). Additionally, the March 2015 monthly-mean freshwater discharge by La Plata River is estimated at $14,600 \text{ m}^3/\text{s}$, as reported by the Argentinean hydrological service (Goniadzki et al., 2015).

We also consider Argo float trajectories from 2005 to 2018 provided by the Coriolis Global Data Acquisition Center of France (<http://www.coriolis.eu.org/>). These floats travel at 1,000 m and, every 10 days, perform a CTD profile between 0 and 2,000 m and transmit these data and position.

Finally, our analysis will benefit from recent reports of velocity time series during 2014–2015 at several cross-slope moorings near 41°S, which sampled the along-slope MC precisely at the same location of our south-western hydrographic stations (Ferrari et al., 2017; Paniagua et al., 2018). The mooring data are available at Saraceno et al. (2017).

3. Inverse Model

3.1. Model Formulation

Under the assumption of a conservative ocean in hydrostatic and geostrophic balance, inverse box models use direct hydrographic observations along the perimeter of an enclosed water volume in order to estimate the ocean circulation (Wunsch, 1978, 1996). Mass conservation is the minimum requirement, although conservation of other physical and biogeochemical properties is often invoked.

The closed volumes for the frontal and confluence models are shown in Figure 1. The frontal area reaches down to only 400 m and is completely locked by the hydrographic stations; the confluence domain reaches much deeper, down to 2,000 m, but is closed to the west by the continental slope. The underlying assumption for the confluence model is that the flow over the slope runs approximately along isobaths, a coastal constraint that holds for poorly stratified flow in geostrophic balance (e.g., Lee et al., 2001); this is consistent with the nearshore orientation of the BCF and SAF, which run parallel to the shelf break while crossing the confluence perimeter. The only exception is the freshwater discharge from La Plata River, which is assumed to enter entirely through the north-western boundary of the confluence region.

We divide the water column in horizontal layers and impose mass and absolute salinity conservation, within uncertainties, for each layer and the entire water column. Between each pair of stations, the horizontal velocity normal to the hydrographic section is the linear addition of the barotropic or reference level velocity (b) and the baroclinic or relative contribution (u_r), the latter inferred from temperature and salinity data through the thermal wind equation:

$$u(s, z) = \frac{g}{\rho_0 f} \int_{z_r(s)}^z \frac{\partial \rho}{\partial s} dz + b(s) = u_r(s, z) + b(s)$$

where (n, s, z) are the coordinates— n pointing out from the domain, s along the perimeter in the counter-clockwise direction, and z in the vertical direction—with corresponding velocity components (u, v, w) ; z_r is the depth of the reference level; ρ is the water density (ρ_0 is a depth-mean density value); g is the gravity acceleration; and f is the Coriolis parameter.

Additionally, we incorporate the mean March 2015 freshwater and Ekman transports to the uppermost layer, in contact with the atmosphere. Either quantity is calculated as a measured value plus a transport adjustment determined by the model, that is, $T_E = \hat{T}_E + \delta T_E$ for the Ekman transport and $F_w = \hat{F}_w + \delta F_w$ for the freshwater input. Part of the freshwater flux corresponds to precipitation minus evaporation, 34×10^{-4} Sv for the confluence region and 8×10^{-4} Sv for the frontal area; the contribution from La Plata River is 14.6×10^{-3} Sv, which adds entirely to either domain through the shelf break. Finally, the Ekman transports along the perimeter of the domain amount to 0.20 and 0.045 Sv for the confluence and frontal domains, respectively.

The mass and property conservation equations for each layer take the following form:

$$\iint_{A_v} \rho C (u_r + b) ds dz + A_h \left[\overline{K \frac{\partial(\rho C)}{\partial z}} - \overline{w \rho C} \right] \Big|_{bot}^{top} + \delta(C) F_w + C T_E = 0$$

where A_h and A_v , respectively, represent the horizontal and vertical areas enclosing an isoneutral; C is the property concentration per unit mass ($C = 1$ for mass); K and w , respectively, are the diapycnal diffusion coefficients and velocities; and $\delta(C)$ is a delta function equal to one when the property is mass and zero otherwise. The overbars in the second term represent mean values at the horizontal areas enclosing the isopycnal layers. The integral accounts for horizontal advection through the lateral limits of the domain, the second term quantifies vertical advection and diffusion (calculated at the upper and lower horizontal areas enclosing the isopycnal layer, taken as zero at the sea surface and the bottom reference isoneutral), and the last two

Table 1
Water Masses in the Confluence Model, Indicating the Corresponding Neutral Density Boundaries and Model Layers (STMW: Subtropical Mode Water, SAMW: Subantarctic Mode Water, AAIW: Antarctic Intermediate Water, UCDW: Upper Circumpolar Deep Water)

Water Mass	Neutral Density (γ^n ; kg/m ³)	Layer
Surface water	Surface–26.2	1
STMW	26.2–26.8	2
SAMW	26.8–27.2	3
AAIW	27.2–27.55	4
UCDW	27.55–27.81	5–6

terms represent the freshwater and Ekman transport terms (entirely in the uppermost isopycnal layer, elsewhere being zero). Each isoneutral or depth level is limited laterally by either the perimeter of the domain or the continental slope, with the intersection of the isoneutrals and seafloor being determined from the World Ocean Database 2013 (<https://www.nodc.noaa.gov/OC5/WOD13/>). To improve the conditioning of the model, the salinity equation is set in terms of anomalies, defined as the difference between the actual value and the layer salinity average (Ganachaud, 2003a; McIntosh & Rintoul, 1997).

In the case of the frontal model, we define five layers using pressure levels (0–50, 50–100, 100–200, 200–300, 300–400 dbar), while in the confluence box we distinguish six neutral density layers, selected on the basis of previous studies (Ganachaud, 2003b; Jullion et al., 2010) (Table 1). Although isoneutral layers appear as a more natural selection, this is unsuitable for the frontal area simply because the densest isoneutral in the subtropical side (about 26.8 kg/m³) reaches very shallow in the subantarctic waters, only down to some 70 m. In contrast, the deepest isoneutral in the confluence region (27.81 kg/m³) everywhere extends deeper than about 1,400 m.

The above partitioning results in six/seven domains for the frontal/confluence models (five/six layers plus the entire domain from the sea-surface to the deepest interface). Considering the number of domains and properties, the frontal/confluence model consists of 12/14 equations (halved between mass and salt anomaly conservation). The 19/28 stations in the frontal/confluence model lead to 18/27 reference velocities, plus 4/5 dianeutral velocities and diffusion coefficients (one for each internal division of the domain) and the freshwater and Ekman transport adjustments. The system is solved using a Gauss-Markov estimator, a method that uses a priori variance information for each unknown (Table 2) in order to produce a minimum error-variance solution with uncertainty estimates (Wunsch, 1996).

3.2. Unknowns and Uncertainties

The reference level for the thermal wind equation is often set at a boundary between two water masses of different origin, which are expected to flow in different directions, where the horizontal velocity is possibly small. However, the BC flows south from the surface down to some 2,000 m (Peterson, 1992) and the MC displays a northward flow over the entire upper slope (Artana et al., 2018). Therefore, we do not expect stable flow reversals within the vertical range of the frontal and confluence models, which burdens setting a proper reference level. Hence, we select the deepest possible reference-velocity level and allow for potentially high reference velocities: for the frontal model we choose 400 dbar, which is the deepest common level to all stations, while for the confluence model we select the deepest common isoneutral in the domain, 27.81 kg/m³, at the base of layer 6 varying between about 1,400 and 2,000 m (Table 1); note that the seafloor becomes the reference level in those slope areas where the water depth or isoneutral reference is not found. The possibility of high reference level velocities is fixed through a relatively large a priori standard deviation, set at 0.3 m/s for both the frontal and confluence domains (Table 2).

The initial dianeutral-velocity estimate at each interface layer is assumed to be zero. Since we are in a region with numerous intrusions and intense mixing, we expect high dianeutral velocities and diffusion coefficients, at least as large as what has been inferred by other authors in an analogous but more extensive geographical domain (Jullion et al., 2010). Hence, we allow fairly high values for the a priori uncertainties of all these variables (Table 2). Finally, the initial estimates for the Ekman and freshwater transports are set to the mean March 2015 values, and the corresponding a priori errors are taken as 50% of these mean values (Table 2).

Table 2
A Priori Information on the Reference-Level Velocity (b), Vertical Diffusion Coefficient (K), Vertical Velocity (w), and Freshwater (δF_w) and Ekman (δT_E) Adjustment Transports for Both the Confluence and Frontal Models

Variable	Initial Value	Standard Deviation
b (m/s)	0	0.3
K (m ² /s)	0	10 ⁻²
w (m/s)	0	10 ⁻⁵
δF_w (Sv)	Mean March 2015 value	50% mean March 2015
δT_E (Sv)	Mean March 2015 value	50% mean March 2015

3.3. Transport Constraints

Several studies have emphasized the barotropic or barotropic-equivalent (considering a 1.5 reduced gravity model) character of the MC (Peterson, 1992; Piola et al., 2013; Vivier & Provost, 1999a, 1999b). Spadone and Provost (2009) and Ferrari et al. (2017) have shown that the ADT-derived surface geostrophic velocities are in good agreement

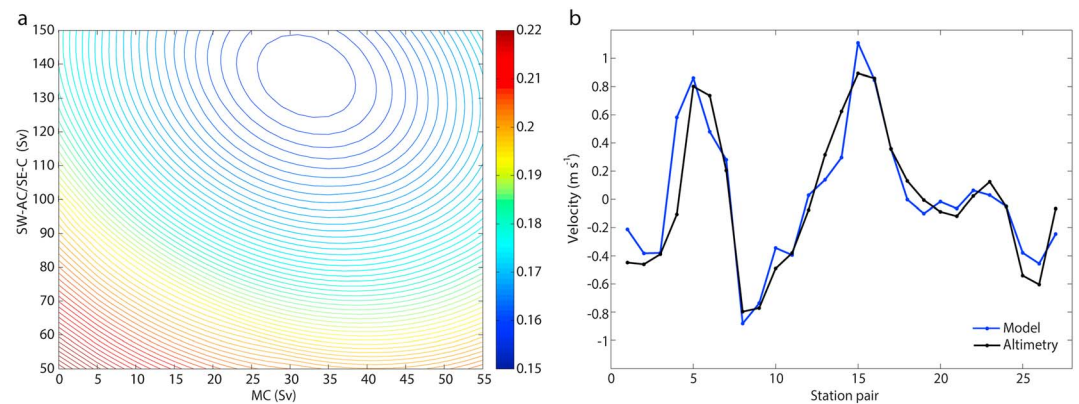


Figure 2. (a) Standard deviation between the inverse-model and altimetry-geostrophic velocities along the confluence perimeter as a function of northward transports in the along-slope MC (stations 1–4) and in the middle of the southern dipole (stations 8–12). (b) Sea-surface velocities from altimetry (black line) and the best fit inverse model (blue line). The abscissa represents station pairs, so that j identifies the flow between stations j and $j + 1$ in Figure 1; negative values represent flow into the confluence domain.

with near-surface measurements from moorings, confirming that the entire water column moves in approximate geostrophic balance. This result has been used in several studies to estimate MC transports in the top 1,500 m of a section which approximately overlaps our first three stations (Artana et al., 2018; Spadone & Provost, 2009; Vivier & Provost, 1999a).

We have looked at the VADCP data along the confluence perimeter to further confirm the goodness of referencing to the altimetry-inferred velocities. A comparison of both velocity fields shows fairly good agreement (the standard deviation is 0.16 m/s in the top 700 m) (Figure S1 and Table S1 in the supporting information); Paniagua et al. (2018) obtained similar results when comparing in situ mooring data with altimetry surface velocities across the MC during 2015. However, the ADCP data are much noisier than the altimetry-inferred velocities, reaching maximum values over the central portion of the eastern part; these peak values are associated with a filament of brackish waters stretching along the frontal zone, which is very likely not in geostrophic balance. Based on these results, we have decided to set the reference level velocities for the confluence model using the information that arises from the sea surface altimetry. Notice that the LADCP data will be used later, to assess the velocities obtained with the inverse model over the entire water column (section 6.1).

Consequently, we constrain the southern flow into the BMC in such a way that the inverse model leads to surface velocities that best fit the altimetry-inferred surface field (at the time of each pair of hydrographic stations). Specifically, we set the integrated transports within those stations where the altimetry-inferred flow is northward—stations 1–4 for the along-slope MC and stations 8–12 in the middle of the southern anticyclonic-cyclonic dipole (Figures 1 and 2)—which then translates into the $\gamma^n = 27.81 \text{ kg/m}^3$ surface reference velocities. The minimum standard deviation corresponds almost exactly to an along-slope MC of 30 Sv and a northward transport of 135 Sv associated to the southern dipole (Figure 2a).

Finally, with the help of the March 2015 mean ADT field (Figure 3), we link the inflow to the frontal area (recall it reaches down to only 400 m) with the water entering the confluence region through the top 400 m. The transports through the upper 400 m of the confluence perimeter are calculated with the velocity fields from the inverse model. We then assume that the ADT contours coincide with the depth-integrated streamlines; that is, the surface connections remain equal at depth (Vivier & Provost, 1999a), and use selected ADT values to connect the flow through the confluence and frontal perimeters. The contours selected are the SAF (0.05 m) and the 0.25 m for the MC inflow, and the BCF (0.30 m), 0.57-, and 0.90-m contours for the BC inflow (Figure S2 and Table S2 in the supporting information). In all cases we allow an a priori uncertainty of 1 Sv.

4. Hydrographic Description

4.1. Surface Circulation

The mean March 2015 sea-surface ADT is characterized by the strangling of the northern portion of the MC, with a significant zonal turn near 42°S, and the double meandering of the BCF, so that the original BCO

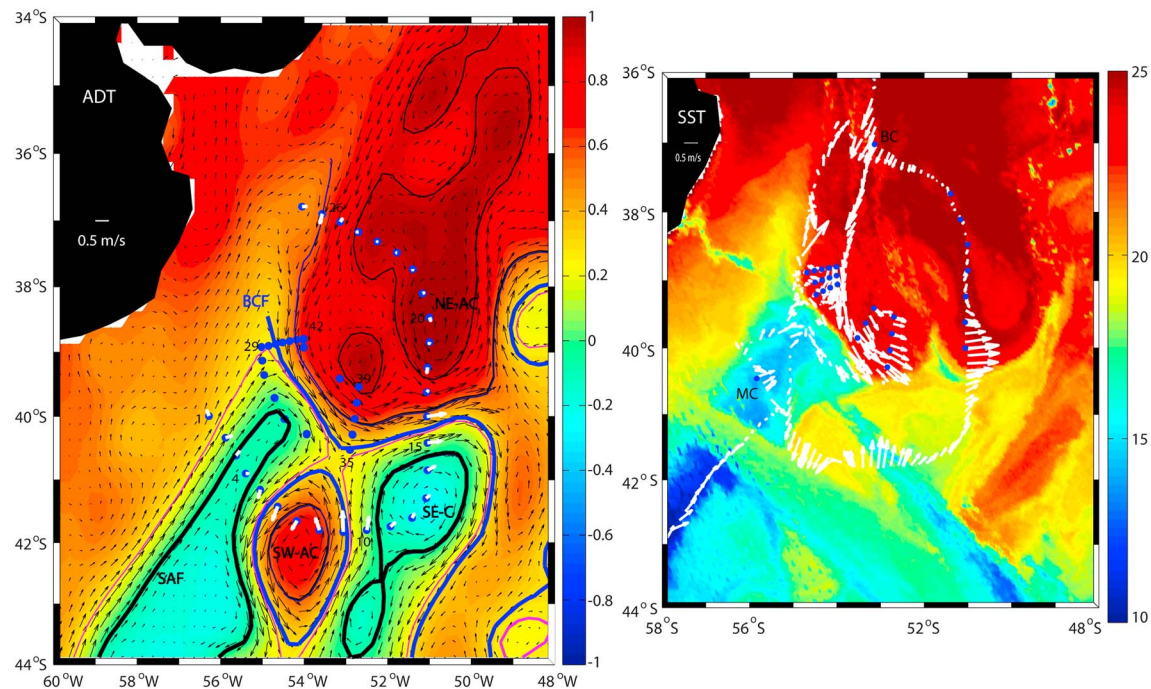


Figure 3. (left) Mean sea-surface ADT (color-coded, in m) and surface velocities in the BMC for March 2015; the black arrows are the velocity vectors as inferred from altimetry and the white arrows denote the velocity vectors at each hydrographic station (blue dots) as obtained from the vessel's LADCP. The black and blue thick lines show the position of the SAF and BCF while the thin magenta, blue, and black lines indicate the 0.25-, 0.57-, and 0.9-m ADT contours, respectively. The southwest anticyclone (SW-AC), southeast cyclone (SE-C), and northeast anticyclone (NE-AC) are identified. (right) SST image for 17 March 2015, together with the 0–700-m depth-averaged VADCP velocity (white arrows) along the vessel's trajectory. The blue dots indicate the location of those stations used to analyze mixing fractions, and BC/MC indicates the positions of those stations used as reference BC/MC water types.

breaks into a large anticyclonic warm eddy (SW-AC; centered at about 42.0°S, 54.0°W) and a warm ridge located further east (along about 49–50°W); these two ADT highs englobe an elongated subantarctic cyclonic eddy (SE-C; centered at about 41.5°S, 51.0°W) (Figures 1a and 3). In the subtropical side of the frontal system, there is another anticyclonic eddy (NE-AC; centered at about 38.5°S, 51.0°W). It is worth emphasizing that all three eddy centers are crossed by those hydrographic stations comprising the confluence perimeter.

The two southern eddies (SW-AC and SE-C) behave as a nonisolated dipole, with a large fraction of water revolving around each eddy and another substantial fraction arriving into or departing from the mesoscale feature (Figures 1a and 3). Regarding the SW-AC, its western flank shows water input from the BCF and output toward the south while its eastern flank has water input from the south and output into the BCF. Analogously, the SE-C feeds partly from water arriving from the south along its western side and partly from water flowing east along the BCF; again, the surface flow associated to the SE-C does not close on itself, as some of it follows south along its eastern margin, away from this cyclone.

A sequence of ADT images prior to the cruise helps appreciate the temporal evolution of the mesoscale features and associated pathways (Figure 4). By the end of January, the SAF appeared as a wide wedge of low ADT values and the MRC-BCO were well defined, corresponding to a characteristic condition of intense MC transport at 41°S (Artana et al., 2018). In contrast, during the second half of February the MRC-BCO flow was disconnected from the frontal system, forming a very large anticyclone. In early March, this large anticyclone broke into two anticyclone structures and the eastern ADT trough became more intense, setting up the dipole that characterizes the weak MC condition at that latitude (Artana et al., 2018).

Considering that the MRC cyclonic (and BCO anticyclonic) recirculation extends far south, around an ADT ridge that stretches all the way to about (46°S, 50°W; Figure 1a), the northward flow along the western margin of the SE-C should belong to a much earlier extension of the MRC-BCO southward flow. Indeed, a surface flow of 0.4 m/s would transit a 1,000-km south-north pathway around this anticyclonic high in about one month. The likely evolution is that of an intense MC and MRC-BCO until mid-February, with high

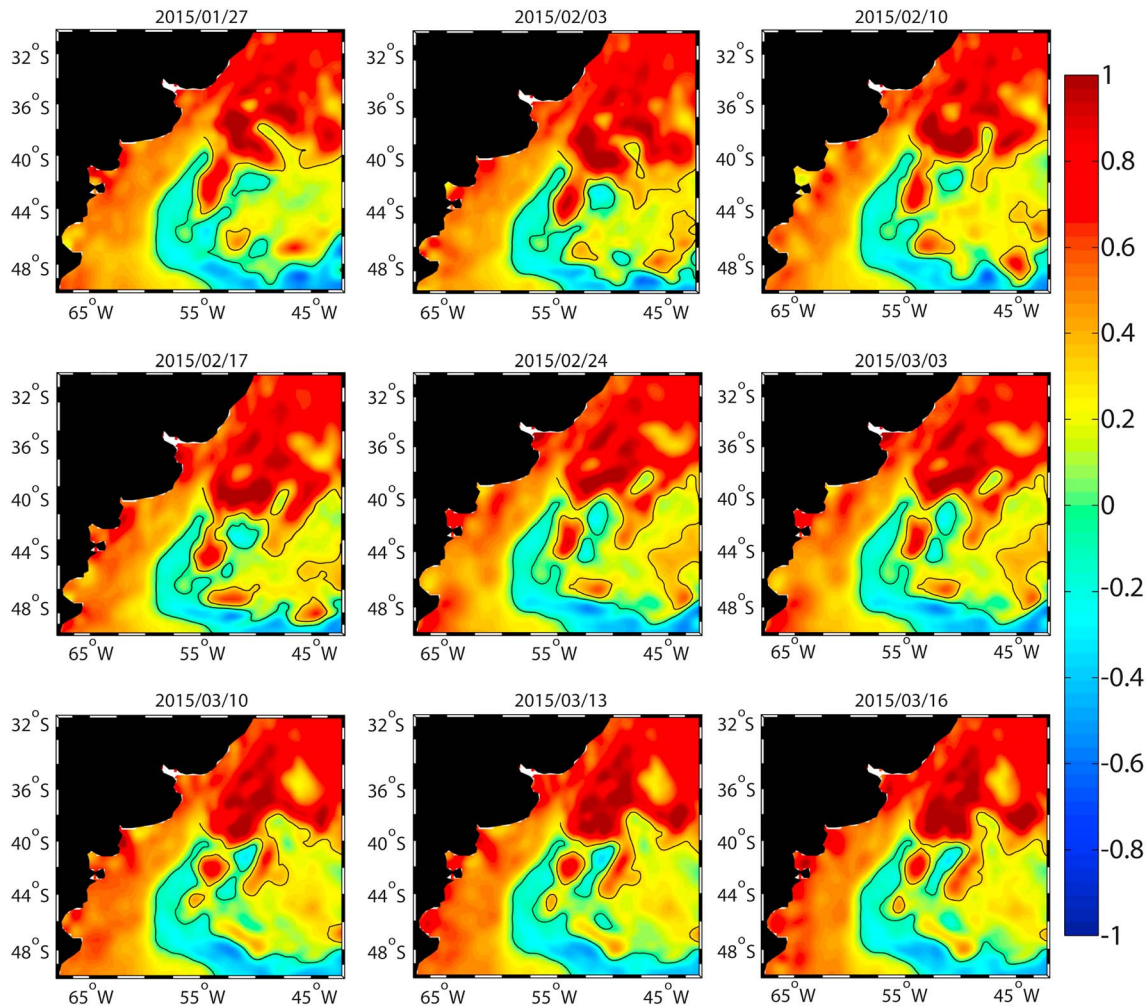


Figure 4. Sea-surface ADT maps (m), weekly from 27 January till 10 March and every three days from 10 to 16 March, together with the position of the SAF and BCF (black lines).

northward and southward flows at least between 45°S and 41°S. In late February, the along-slope MC weakened at higher latitudes as an eastern diversion appeared near 45°S that connected with the intense interior northward flow near 53°W (through the middle of the dipole); we will come back to these ideas in section 6.2.

4.2. Water Masses and Vertical Sections

Six water masses appear in the upper 2,000 m of the BMC (Maamaatuaiahutapu et al., 1992; Figure 5). In the surface layers of several stations we find low-salinity and warm waters with a substantial contribution from La Plata River. In the thermocline and intermediate layers we identify four water masses (Table 1): salty and warm Subtropical Mode Water (STMW; $S = 36\text{--}37$ g/kg, $\theta = 15\text{--}23$ °C, $\gamma^t = 26.2\text{--}26.8$ kg/m³, $z \cong 50\text{--}300$ m), fresh Subantarctic Mode Water (SAMW; $S \cong 34.4$ g/kg, $\theta = 5\text{--}8$ °C, $\gamma^t = 26.8\text{--}27.2$ kg/m³, $z \cong 100\text{--}650$ m), fresh and cold Antarctic Intermediate Water (AAIW; $S \cong 34.3$ g/kg, $\theta \cong 3$ °C, $\gamma^t \cong 27.2\text{--}27.55$ kg/m³, $z \cong 800\text{--}1,500$ m), and low-oxygen Upper Circumpolar Deep Water (UCDW; $S \cong 34.7$ g/kg, $\theta \cong 2.8$ °C, $\gamma^t \cong 27.55\text{--}27.92$ kg/m³). Below 1,800 m, but only in station 4 and within the SE-C, we find North Atlantic Deep Water ($S > 34.8$ g/kg, $\theta = 2.0\text{--}3.5$ °C, $\gamma^t > 27.92$ kg/m³).

Asides the surface waters, in the entire domain there are subantarctic mode and intermediate waters plus UCDW, with an abrupt transition from subantarctic (fresher, colder, and denser) to subtropical (warmer, saltier, and lighter) waters across the BMC. This transition is clear in the distribution of temperature and salinity along vertical sections following the perimeters of the frontal and confluence domains (Figure 6;

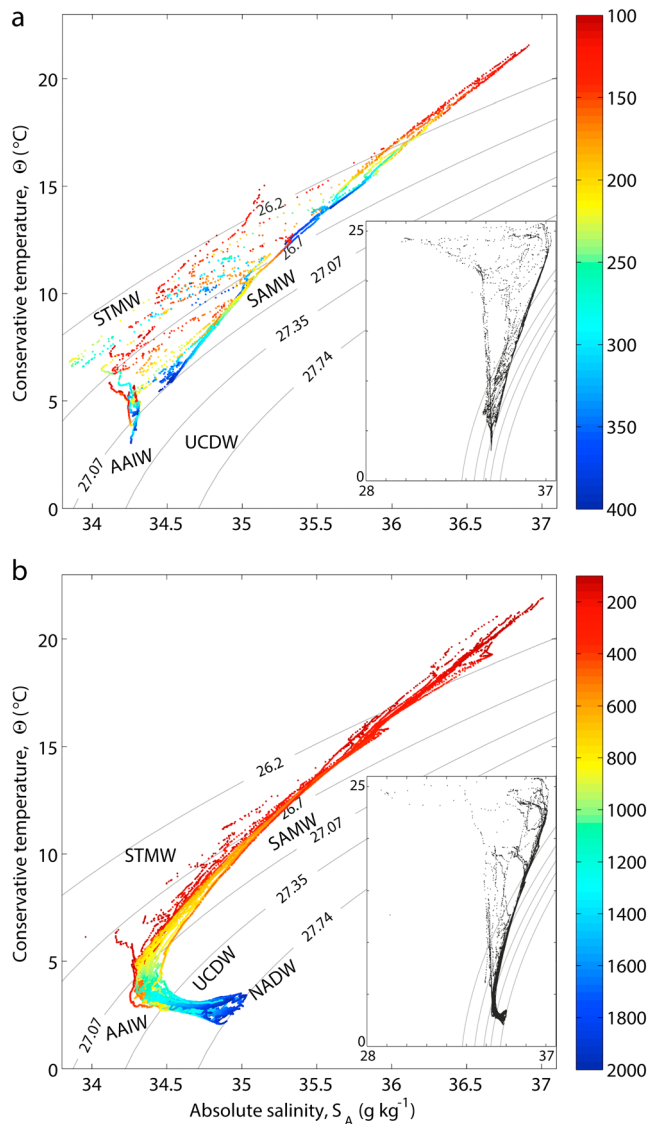


Figure 5. Conservative temperature–absolute salinity diagrams for the frontal and confluence domains. (a) The frontal diagram includes data from 100 to 400 m while (b) the confluence diagram uses all data between 100 and 2,000 m (the inner panels include data in the top 100 m). The plots are color-coded with depth (m), with the gray lines showing the isopycnals (kg/m^3) that approximately delimit the water-mass layers used in the confluence model.

recall that the 400-m-deep frontal perimeter closes on itself while the 2,000-m-deep confluence perimeter remains open along the shelf break. Considering this distribution of water masses, we may safely say that our inverse-model transports encompass all surface, mode, and intermediate waters plus most of the UCDW.

In the frontal area (Figures 6a and 6b), the southern rim is dominated by subantarctic waters, the northern edge by subtropical waters, and the eastern and western sides display a remarkably steep frontal structure (the slope of the 26.8 kg/m^3 isoneutral is about 10^{-2}). The entire area presents a very shallow (everywhere less than 10 m) warm and relatively fresh layer (temperatures over 15°C and salinities less than 34 g/kg), caused by the runoff from La Plata River. Additionally, the upper waters of the subantarctic side reflect summer warming, that is, temperatures over 7.5°C down to about 50 m, and the frontal system displays thermohaline intrusions of cold subantarctic waters at different levels, particularly intense near the slope.

The temperature and salinity distributions along the perimeter of the confluence region delimit the vertical extensions of the STMW, down to 26.8 kg/m^3 or about 600 m. The subantarctic waters along the southern edge of the confluence domain are crossed by the large SW-AC (diameter about 200 km), which is almost entirely formed by STMW; the 26.8 kg/m^3 isoneutral in this eddy is somewhat shallower, about 400 m, which is the same depth reached by this isoneutral in the frontal area. The MC (stations 1–4) is mostly occupied by AAIW and UCDW (from about 200 to 1,700 m), showing (θ, S) values similar to those characterizing weak MC conditions (Paniagua et al., 2018). The eastern cyclone (SE-C), of subantarctic origin, appears relatively isolated during the cruise but the time sequence of ADT images (Figure 4) shows that it belongs to an earlier northward return of the MRC; its long transit over the region is reflected by a relatively deep, warm, and fresh surface layer.

The vertical section along the confluence perimeter also shows that all deep isoneutrals follow the same shape as the 26.8 kg/m^3 isoneutral, that is, replicating the base of the STMW down to at least 2,000 m. This is consistent with the idea that these subantarctic waters have a relatively small baroclinic contribution. This is true even in the north-western end of the perimeter, where the modal and intermediate waters shallow toward the slope, suggesting the existence of a southward along-slope flow at these deep levels.

4.3. Baroclinic Transports

We may calculate the geostrophic transports in and out the frontal and confluence domains without use of the inverse model, that is, maintaining null reference velocities and vertical exchange. The net transport imbalances into either domain will indicate the size of the transports that need to be accommodated by the inverse model.

We use the BCF in order to partition either perimeter into two segments (south and north of the BCF) where the water flow is of southern and northern origin. For each segment and layer, we separately add up all water transports in and out of the domain (recall positive values represent flow divergence; Figure 7); the transports entering each segment will provide our first estimate of the baroclinic transports by the MC and BC in the upper 2,000 m of the water column.

In the frontal model, the depth-integrated inflow (outflow) is -2.5 Sv (6.3 Sv) for the southern segment and -5.4 Sv (1.7 Sv) for the northern segment, for net imbalances of 3.8 and -3.7 Sv , respectively. In the confluence model, the depth-integrated inflow (outflow) is -49.1 Sv (71.4 Sv) for the southern segment (most of it

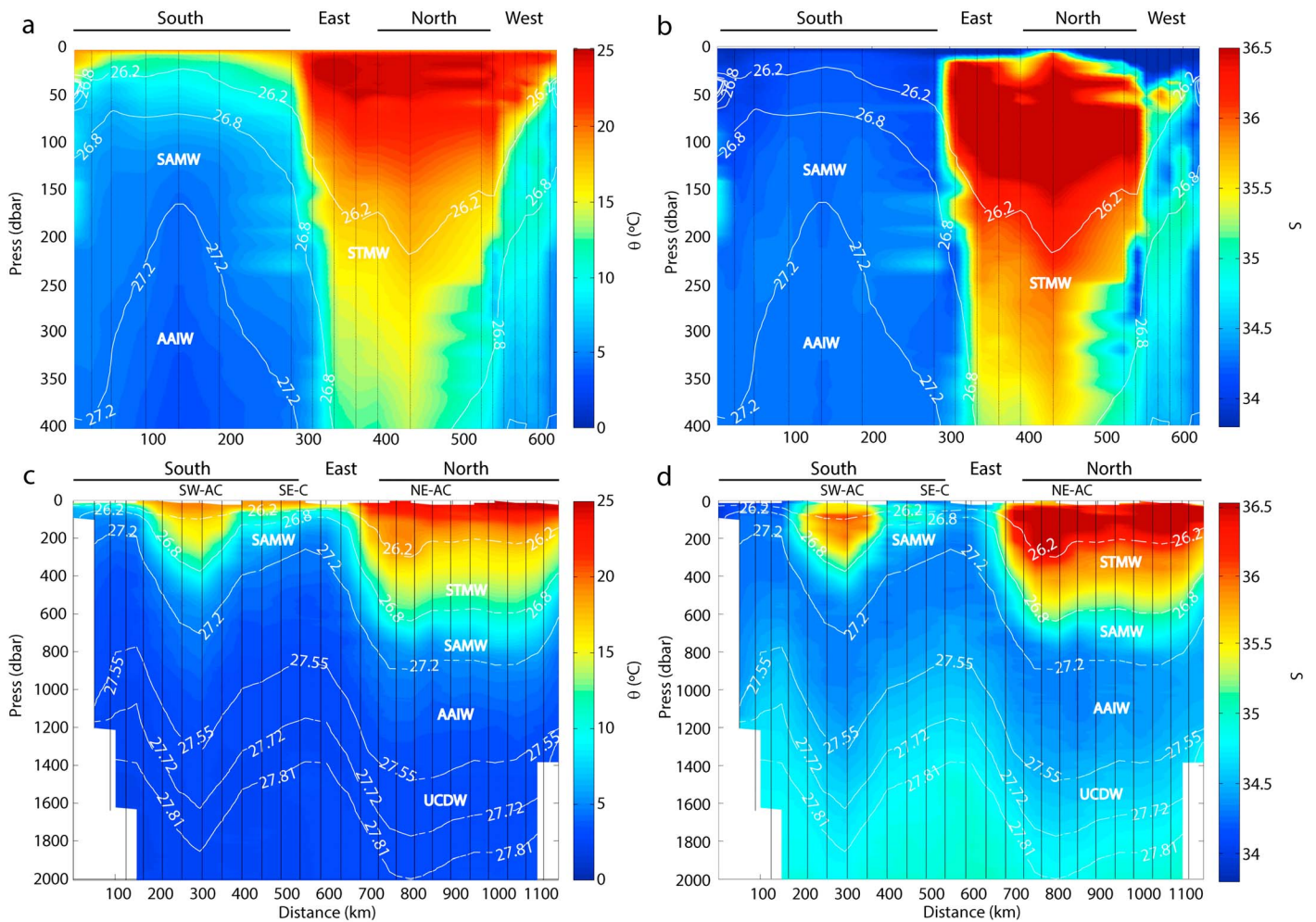


Figure 6. (a and c) Vertical sections of conservative temperature θ (°C) and (b and d) absolute salinity S (g/kg) for the (a and b) frontal and (c and d) confluence models. The white lines represent the isoneutral water-mass boundaries used in the confluence inverse model and the black dots indicate the data points, and the water masses are labeled according to the boundary definitions in Table 1. The southern, eastern, and northern edges follow those sectors shown in Figure 1b, and the approximate extent of the mesoscale eddies is indicated.

in the AAIW stratum) and -45.6 Sv (38.4 Sv) for the northern segment (dominated by the surface and STMW strata), for net imbalances of 22.2 and -7.2 Sv, respectively. The total imbalance for the entire frontal area is very small, only 0.2 Sv, while for the confluence region it is 15.0 Sv (10.6 Sv in the SAMW and AAIW layers). The large input–output differences through the southern and northern segments of the frontal and confluence perimeters are difficult to justify. Further, the imbalance for the confluence model doubles the water inflow associated to the along-slope MC. Both discrepancies plenty justify the use of the inverse model.

5. Model Results

We now turn to the results of the inverse model for both the confluence and frontal domains. In either case we present the velocities normal to the perimeter (Figure 8) as well as the transports into or out of the domain and the transports accumulated along the perimeter (per layer and total; Figures 9 and 10).

5.1. Confluence Model

Water enters the confluence region via both the MC in the southwestern edge and the BC in the northern side, and output occurs at the southern and southeastern margins (Figure 8c). The pattern of water inflow and outflow in the southern side actually reflects the existence of the along-slope MC, the recirculations associated with the SW-AC and SE-C dipole, and the southern sources and sinks for this dipole (Figure 3).

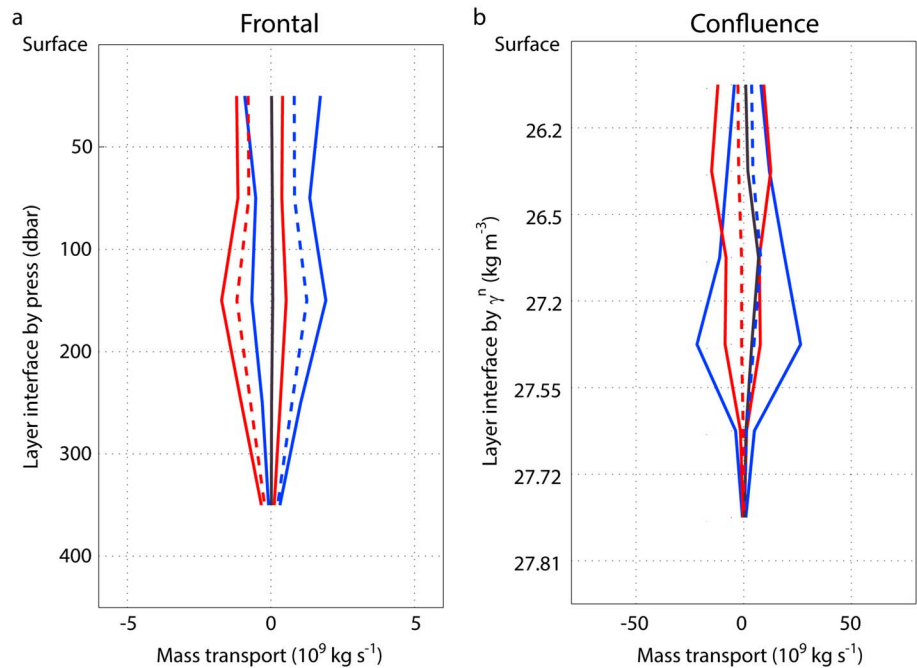


Figure 7. Baroclinic mass transports in the (a) frontal and (b) confluence models. The transports are calculated independently for the southern (blue) and northern (red) segments, which are separated by the BCF. Further, all flow into and out of the box is computed separately, with negative (positive) values indicating the flow entering (leaving) the domain; the dashed lines (blue for the southern segment and red for the northern segment) represent the differences between the flow leaving and entering each domain. The black line represents the net transport for the entire box.

The reference velocities at 27.81 kg/m^3 are fairly large in all stations south of the BCF (up to about 0.4 m/s in stations 8 to 11), with negative values (water input) in those places where northward transport is imposed (stations 1–4 and 8–12; section 3.3) and positive values elsewhere, confirming the barotropic character of the MC and associate recirculations. In contrast, the reference level velocities are small for all stations north of the BCF, indicating that most of the transport associated with the BC is baroclinic in the upper 2,000 m (Figure 8d).

The vertical velocities range between 10^{-7} and 10^{-6} m/s , leading to relatively minor vertical mass transports between adjacent layers (Figure S3 in the supporting information). The largest vertical transport takes place from the SAMW to the AAIW layers, accounting for $1.2 \pm 1.5 \text{ Sv}$; however, because of the large a priori uncertainties, it is not significant. The vertical diffusion coefficients, which cause no water transport but do contribute to the salt balance, are on the order of $10^{-5} \text{ m}^2/\text{s}$, neither significant (Figure S3 in the supporting information).

We can use the BCF to distinguish between the transports associated to the MC and BC for each segment and layer (Figure 9b). The mass conservation condition is fulfilled for every layer; that is, the transport uncertainties are larger than the residuals, though barely in the SAMW and AAIW layers. The total imbalance for the confluence region is -0.01 Sv . The very large southern transports in the AAIW, and to a lesser degree in the SAMW and UDCW layers, are a reflection of the recirculations associated with the two eddies south of the BCF. The net transports (inflow minus outflow) are relatively small for each segment and layer, always less than 2 Sv except in the southern segment for the AAIW, where there is a net inflow of $6.5 \pm 2.0 \text{ Sv}$. In the northern segment, the largest transports occur in the top two layers (surface and STMW), although the largest imbalance is for AAIW, with a net loss of $3.1 \pm 2.8 \text{ Sv}$.

These results are complemented with the cumulative transports per layer, starting at the southwestern corner (Figure 10b; recall that there are no stations along the shelf break). The MC contributes with $28.3 \pm 1.4 \text{ Sv}$ along the slope and there are as much as $87.6 \pm 10.6 \text{ Sv}$ flowing south along the western margin of the SW-AC. Assuming that the flows are connected and in steady state, the difference between these two

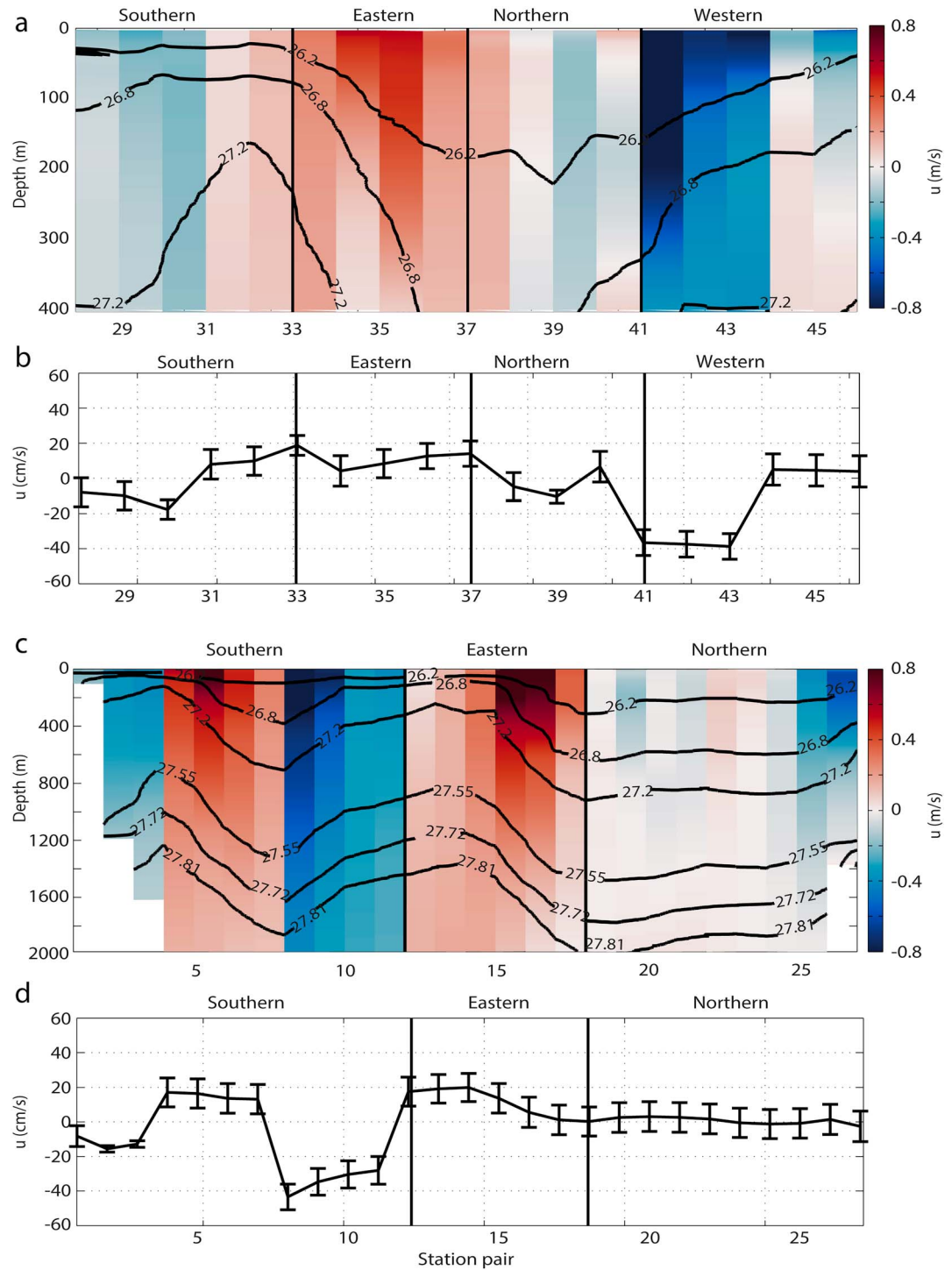


Figure 8. Vertical distribution of the inverse-model velocity through the along-perimeter section for the (a) frontal and (c) confluence models. Reference-level velocities along the perimeter for the (b) frontal (at 400 m) and (d) confluence (at the 27.81 kg/m^3 isoneutral) models. Negative/positive (blue/red) values denote inflow/outflow velocities. The southern, eastern, and northern edges follow those sectors shown in Figure 1b, and the abscissa represents stations pairs, as in Figure 2.

values tells us the maximum water transport that recirculates within the SW-AC, $59.3 \pm 10.7 \text{ Sv}$; note that this is a maximum value because some water may continue further south, away from the anticyclone. Further east, along the eastern (western) side of SW-AC (SE-C), there is a northward transport of

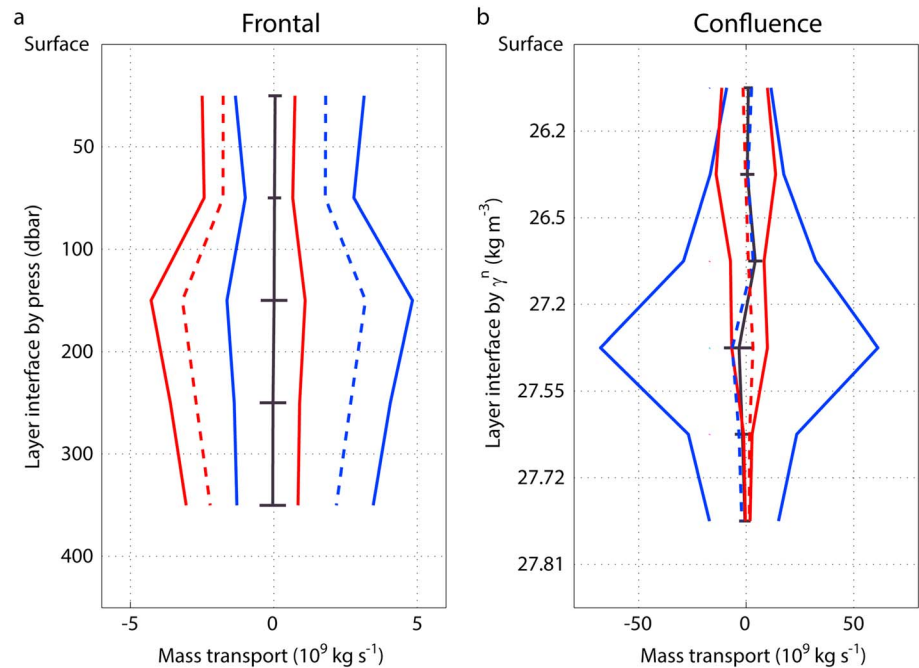


Figure 9. Mass transports in the (a) frontal and (b) confluence models as deduced from the inverse model (notation as in Figure 7).

138.2 ± 1.0 Sv. Subtracting the maximum water recirculating within the SW-AC, this gives an additional inflow of at least 78.9 ± 13.7 Sv, possibly even more. The major contribution to water transport in this southern segment corresponds to AAIW, accounting for about 40% of the total transport at each location.

North of the BCF, there is a total inflow of 35.9 ± 6.2 Sv; however, because of a local cyclonic recirculation (5.1 Sv), the net inflow accounts for only 30.8 ± 12.0 Sv, with an along-slope input of 29.1 ± 8.3 Sv (Figure 10b). This net transport is split, roughly in equal parts, among subtropical (STMW) and subantarctic (SAMW and AAIW) waters. The southern (78.9 Sv) and northern (30.8 Sv) net inflows are eventually drained out of the confluence region through the eastern border, with a total of 109.7 ± 15.1 Sv. Part of this eastward flow will continue northward as the BC offshore recirculation, another will form the SAC and continue eastward, and another one flows southward and feeds the SE-C as will be discussed in section 6.2.

5.2. Frontal Model

Water enters the frontal area via the MC in the western half of the southern margin and via the BC in the western and, to a lesser degree, northern borders; the outflow takes place mostly through the eastern half and, to a lesser degree, through the eastern portion of the southern and northern sides (Figure 8a). The reference velocities are fairly large in stations 28–32, influenced by the MC, and stations 41–44, forced by the BC; they also reach large values in some of the southeastern and eastern stations, where intense outflow takes place.

The inverse model also shows that the vertical velocities are of order 10^{-7} m/s, leading to nonsignificant net vertical mass transports between adjacent layers (Figure S3 in the supporting information). The vertical diffusion coefficients are on the order of 10^{-4} m²/s, again not significantly different from zero (not shown).

We again use the BCF to quantify the transports associated to the MC and the BC segments, in and out per segment and layer (Figure 9a). The main exchanges with the confluence region occur in the top 200 m. Mass output is higher than input along the southern flank while the opposite occurs in the northern flank. The net imbalance for the entire frontal area is of only -0.05 Sv.

The relatively intense recirculation pattern in the shallow frontal area arises after we constrain the flow through the perimeter of the confluence region to follow the ADT-streamlines into the frontal boundary (section 3.3). Without this constraint the southern and northern inputs into the frontal area were 2.0 and

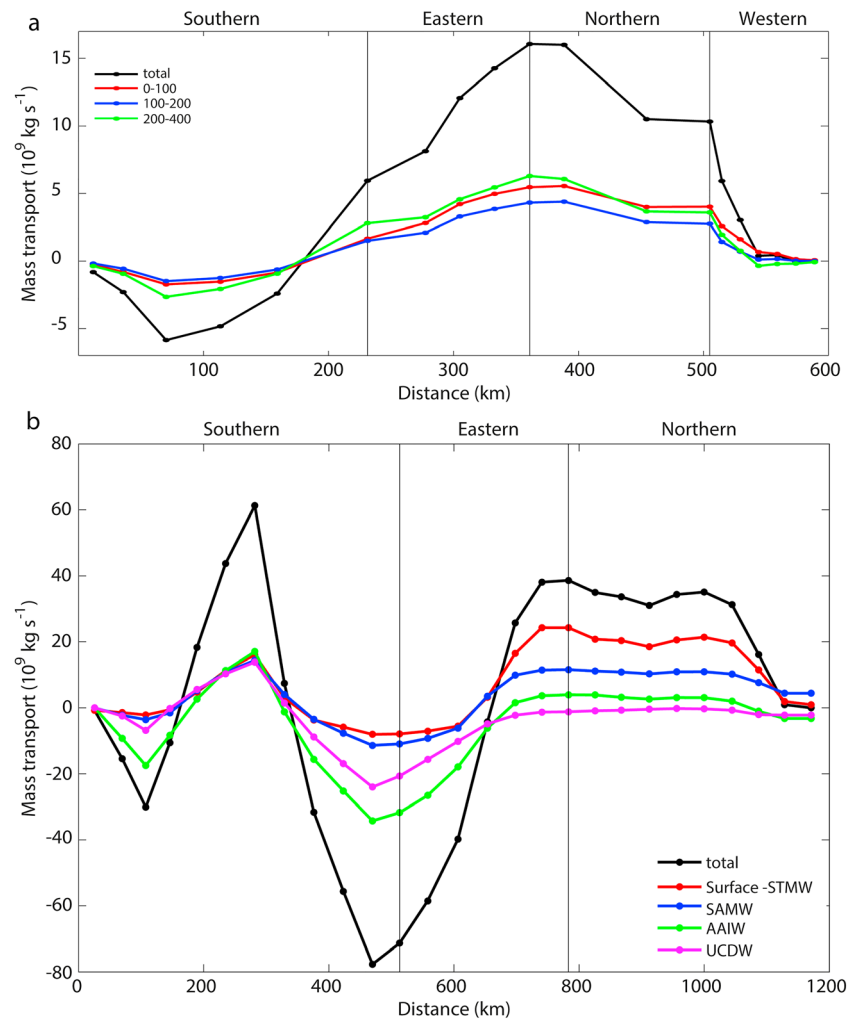


Figure 10. Accumulated mass transports, per layer and total, for the (a) frontal and (b) confluence models. The transports for the several frontal and confluence layers are color-coded with negative values indicating transports into the box. The southern, eastern, and northern edges follow those sectors shown in Figure 1b.

–5.4 Sv, respectively (Figure 7). After constraining the flow with the help of the mean March ADT, these transports increase largely, with a southern input of 6.6 ± 1.5 Sv and a northern contribution of 15.9 ± 0.8 Sv (Figure 9).

The cumulative transports provide a complementary view of the exchange of water within the frontal area (Figure 10a). Beginning at its southwestern corner, after an input of 5.9 ± 1 Sv through the southern border, there is an outflow of 21.9 ± 1.7 Sv in the southern and eastern borders. This difference is accounted by inflow through the northern (5.7 ± 1.5 Sv) and western (10.4 ± 0.9 Sv) sides. About half of the input/output occurs in the top 100 m and the other half is split roughly equal in the 100–200- and 200–400-m levels.

6. Discussion

6.1. Comparison of Inverse Model and ADCP Fields

One natural alternative to the inverse model would be the ADCP data. However, these measurements may incorporate large errors in areas of weak acoustic backscattering, such as in the deep ocean, or high instrumental tilt (heading, pitch, and roll), as in the presence of strong currents (e.g., King et al., 2001; Ott, 2002; Polzin et al., 2002; Thurnherr et al., 2017). Nevertheless, since the inverse model solution has been possible

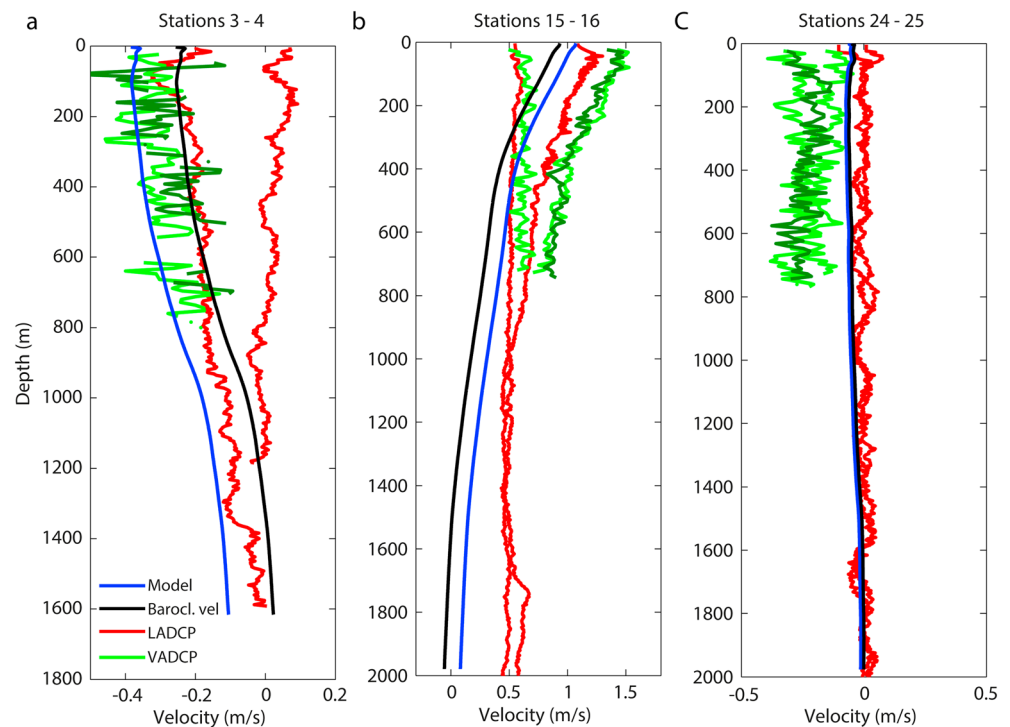


Figure 11. Velocity samples from three station pairs: baroclinic contribution referenced to the 27.81-kg/m^3 isoneutral (black) and inverse model (blue) velocities at the midpoint between both stations and normal-to-section velocities with the LADCP at both stations (red) and with the VADCP at both stations and the central point (green, darker green for the midpoint profile).

with no need of in situ velocity measurements, it is appropriate to compare the inferred velocity fields with both the LADCP and VADCP values (the latter in the top 700 m).

For the model-measurement comparison, we must keep in mind that inverse-model velocities are calculated at the midpoints between hydrographic stations, the LADCP velocities are at the stations, and the VADCP provides near-continuous values along the ship track. In Figure 11 we compare the velocities for selected stations in the southwestern (3–4), eastern (15–16), and northwestern (24–25) edges of the confluence model. In each case we have up to seven velocity profiles: the baroclinic contribution (determined through the thermal wind equation with zero reference velocity) and the inverse model prediction at the midpoint between stations, LADCP data at the two adjacent stations, and the VADCP data computed both at the stations and at the midpoint (for the comparison we always use the component of the LADCP and VADCP velocities normal to the section).

The results in Figure 11 illustrate the type of discrepancies among the several data sets and the model, showing the potential limitations if we were to use only the ADCP measurements. The VADCP velocities are always the noisiest. Most remarkable, we find several instances where the velocities are substantially different when sampled at one same location with different instruments (e.g., stations 24–25) or when sampled at adjacent locations with one same instrument (e.g., VADCP in stations 15–16 or LADCP in stations 3–4).

Using the normal-to-section LADCP velocity component, we may construct velocity sections that are suitable for direct comparison with the inverse model velocities (left panels in Figures 12a and 12c). The LADCP velocities reproduce the same patterns as deduced with the inverse model but with generally higher speeds, particularly in the eastern section. The velocity difference between the LADCP and the model is rather intermittent, with a standard deviation of 0.1 m/s, although the velocity difference in the eastern section can locally be as large as 0.4 m/s (right panels in Figures 12a and 12c).

The LADCP velocity near the reference level (Figures 12b and 12d) is calculated as the average velocity in the 360- to 400-m range along the frontal perimeter and within 200 m from $\gamma^{\theta} = 27.81\text{ kg/m}^3$ along the confluence limit. Despite the LADCP and model velocities display similar spatial trends, there are large differences

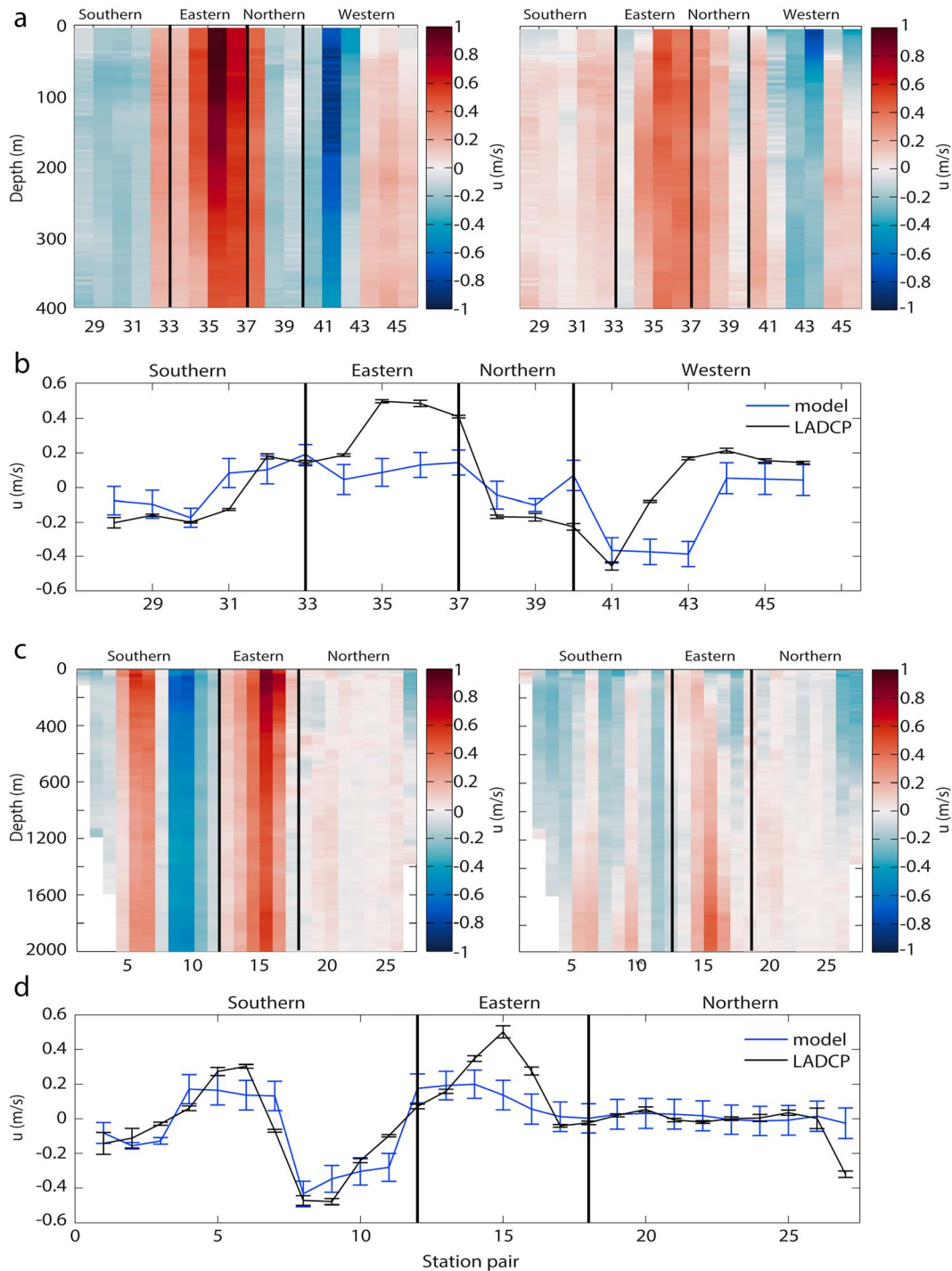


Figure 12. Normal-to-section velocities along the (a and b) frontal and (c and d) confluence perimeters; the southern, eastern, northern, and western edges (the latter only for the frontal area) follow those sectors shown in Figure 1b, and the abscissa represents station pairs, as in Figure 2. (a and c) The left panels show the vertical distribution of the LADCP velocity and the right panels show the difference between the LADCP and model velocities; the negative/positive values denote inflow/outflow velocities. (b and d) Pseudo reference-level velocities (black line) are calculated along the perimeters as explained in the text and compared with the model solution (blue line).

in the western and eastern transects of the frontal model (Figure 12b) and in the eastern transect of the confluence model (Figure 12d), leading to a substantial standard deviation (0.25 m/s).

The velocity differences between the model and the LADCP, throughout the entire water column and particularly at the reference level, peak in zones of high surface velocities, where the rosette-CTD-LADCP

system experienced substantial tilt and the ship drifted large distances during the cast, degrading the quality of processed LADCP velocities. This is the case in the eastern sections of both the frontal (stations 35–36) and confluence (stations 15–16) perimeters, where the frontal area was accompanied by a swift filament of brackish waters (depths less than 30 m). Hence, it seems plausible that these high local LADCP bottom velocities are defective, pointing at the need of using the inverse model.

Differences between the model and ADCP velocities may also result from the limited spatiotemporal resolution of the altimetry data (e.g., Pascual et al., 2013) when constraining the flow or simply because the velocity field may have high nongeostrophic local contributions; for example, both effects may add up in the relatively narrow surface brackish filament that flows along the BCF, causing the altimetry-inferred speeds to be much weaker than the VADCP values (Figure S1 in the supporting information). However, notice that the error in transport over a restricted number of stations associated with a swift but shallow (<50 m) and narrow (<50 km) filament out of geostrophic balance would be relatively small (a velocity error of 0.4 m/s would cause a transport error less than 1 Sv), much less than the transport error for the entire water column due to a flawed bottom velocity of only 0.1 m/s (for a water column of 1,400 m this would represent 28 Sv).

6.2. Baroclinic, Barotropic, and Total Transports

Our results for the upper 2,000 m of the water column show very different situations north and south of the BCF. North of the BCF we find the BC, a highly baroclinic current with weak velocities at $\gamma^n = 27.81 \text{ kg/m}^3$. Further, as the BC approaches the BMC, it experiences feeble interior-ocean recirculations; that is, there are no cyclonic eddies north of the BCF and the anticyclonic eddies are of moderate strength. In contrast, south of the BCF we find much higher reference velocities at 27.81 kg/m^3 , reaching 0.4 m/s in the northward flow at the middle of the southern dipole, confirming a very substantial barotropic contribution. Additionally, the flow in this southern region displays intense mesoscalar structures; that is, there are several cyclonic and anticyclonic features south of the BCF: the cyclone formed by the MC and MRC, an anticyclone that replaces the BCO, and an interior-ocean cyclone.

Figure 13 shows the local transports (between each station pair) associated with each water mass in the confluence model. These transports, which delineate the contributions by the boundary currents as well as the interior recirculations, are drawn on top of the surface geostrophic velocity field. In this figure we have also included the barotropic and baroclinic contributions down to $\gamma^n = 27.81 \text{ kg/m}^3$ for the major pathways crossing the BMC: the along-slope MC and MRC, the SW-AC, the interior northward flow through the middle of the SW-AC and SE-C dipole, the outflow along the BCF, and the along-slope inflow and interior recirculations of the BC. These numbers illustrate the contrast between a MC with substantial barotropic transports and a BC that is essentially baroclinic, and further emphasize the northward inflow near 53°W and the eastward outflow along the BCF (Table 3).

The along-slope BC transport ($29.1 \pm 8.3 \text{ Sv}$) agrees, within uncertainties, with previous estimates ranging between 20 and 44 Sv (Garzoli et al., 2013; Maamaatuaiahutapu et al., 1998; Peterson, 1992; Zemba, 1991). Most of the BC transport is baroclinic: 29.0 Sv in the upper 2,000 m as opposed to only 0.1 Sv associated with the $\gamma^n = 27.81 \text{ kg/m}^3$ reference velocity. This very small barotropic contribution is consistent with the weak southward transport (2 Sv) obtained by Goni et al. (1996).

The transport of the along-slope MC is $-28.3 \pm 1.4 \text{ Sv}$, below earlier estimates for this current, in the order of 35–60 Sv (Saunders & King, 1995; Spadone & Provost, 2009; Vivier & Provost, 1999a), but not so far from the potential variability calculated by Artana et al. (2018) from the combined analysis of 25 years of altimetry and mooring data at 41°S, $37.1 \pm 6.6 \text{ Sv}$. The baroclinic contribution relative to $\gamma^n = 27.81 \text{ kg/m}^3$ (-13.3 Sv) is on the order of previous estimates when assuming a level of no motion at 1,400 m (Garzoli, 1993; Gordon & Greengrove, 1986), although much less than the 23 Sv estimated by Vivier and Provost (1999b) using this same reference level. The barotropic and baroclinic contributions are fairly equal, 53% and 47%, in agreement with Vivier and Provost (1999b). Therefore, the constraints imposed onto the three southwestern stations of the confluence perimeter (section 3.3) reproduce correctly the important barotropic inflow in the MC.

According to the time series reported by Artana et al. (2018), the MC at 41°S was unusually weak between December 2014 and August 2015, with near-average transports between mid-January and the end of April 2015 (35–37 Sv) and much weaker between May and August. From the analysis of velocity, salinity, and

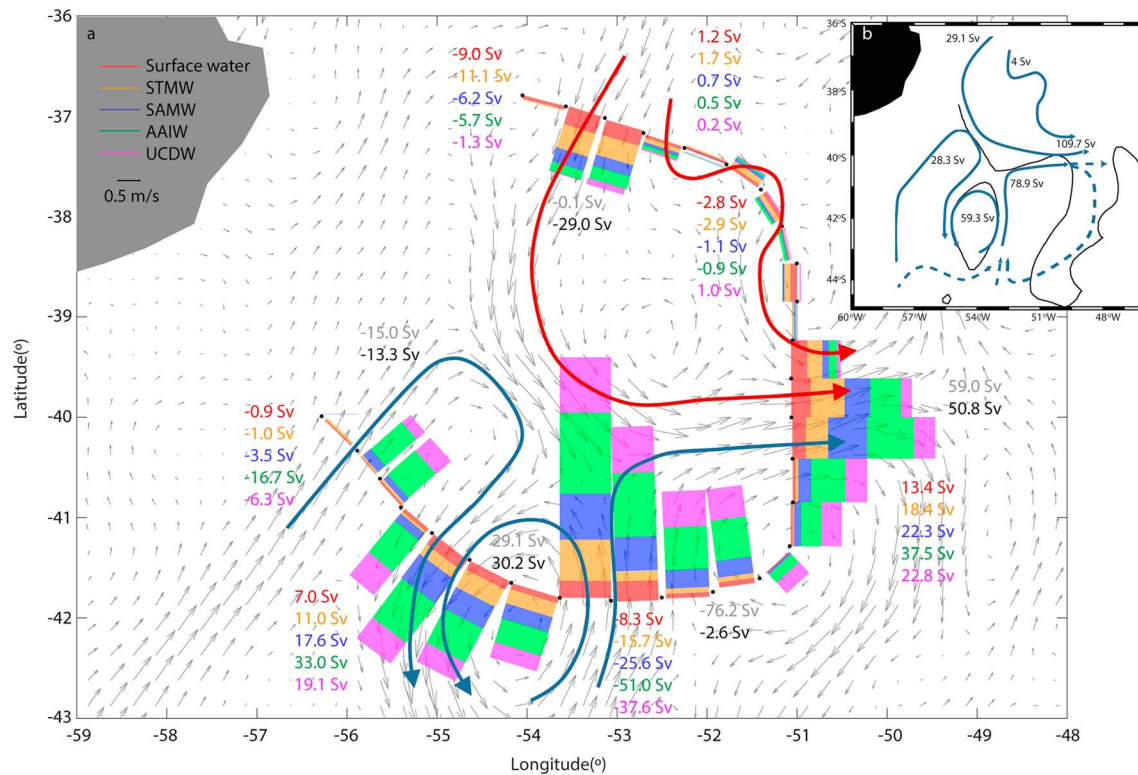


Figure 13. (a) Transports per water mass and for each station pair as inferred from the inverse model. The color bars illustrate the partitioning of the transports among different water masses (surface, red; STMW, orange; SAMW, blue; AAIW, green; UCDW, magenta) and the colored numbers refer to the depth-integrated transports between those stations where the transport changes sign. The lines depict the major currents and the associated numbers indicate the barotropic (gray digits) and baroclinic (black digits) contributions. The vectors (gray arrows) represent the surface geostrophic velocities as inferred from the altimetry. (b) Scheme of the main currents (solid lines) and associate transports, together with the proposed MC interior pathways (dashed lines); the BCF is shown as a black line.

temperature variations during 2015 from mooring data along this same 41°S line, Ferrari et al. (2017) and Paniagua et al. (2018) classified the January–April period as strong; however, considering Artana et al.’s (2018) results, this strength is relative to the very weak MC conditions that took place between May and August 2015. Close inspection of Paniagua et al.’s (2018) velocity time series further shows that the along-slope flow experienced a substantial decrease during the first 10 days of March 2015, which caused a short reversal of the along-slope-flow orthogonal function.

The mean ADT pattern in March 2015 (Figures 1a and 3) indeed resembles the characteristic ADT distribution at times of minimum MC near the BMC (Artana et al., 2018): the SAF is at a southern position, the BCO has split into an anticyclonic eddy, and the MRC at 46°S is connected with the interior-ocean cyclonic structure. The dipole formed by the SW-AC and the interior SE-C appears as a remarkable feature at the time of the cruise. The northward flow between both eddies is particularly strong as it accounts for the recirculation within the SW-AC (59.3 Sv) and an additional very intense inflow (78.9 Sv). This strong interior northward flow near 53°W (hereafter to be referred as interior northward flow) cannot be solely explained in terms of a time delay in the arrival of an earlier along-slope MC, simply because the January–February transport did not exceed 37 Sv (Artana et al., 2018).

We may explore if the existence of the interior northward flow can be sustained via meridional pathways from more southern latitudes. A preliminary analysis of along-slope Argo trajectories between 45°S and 50°S sustains the possibility of this interior pathway. We find that a substantial fraction of these floats, roughly one third of all floats, divert from the slope much before reaching the BMC. Figure 14 shows 10 float trajectories that display such behavior, with half of them diverting cyclonically near 42°S

Table 3
Model Barotropic, Baroclinic, and Total Contributions (in Sv), Relative to $\gamma^{\theta} = 27.81 \text{ kg/m}^3$, for the Major Pathways Reaching the Confluence Region (Negative/Positive Values Refer to Inflow/Outflow); the Transports for SW-AC and SE-C Are Maximum and Minimum Values, Respectively

	Baroclinic	Barotropic	Total
MC	-13.3	-15.0	-28.3
SW-AC	30.2	29.1	59.3
SE-C	-2.7	-76.2	-78.9
SAC	50.8	58.9	109.7
BC	-29.0	-0.1	-29.1

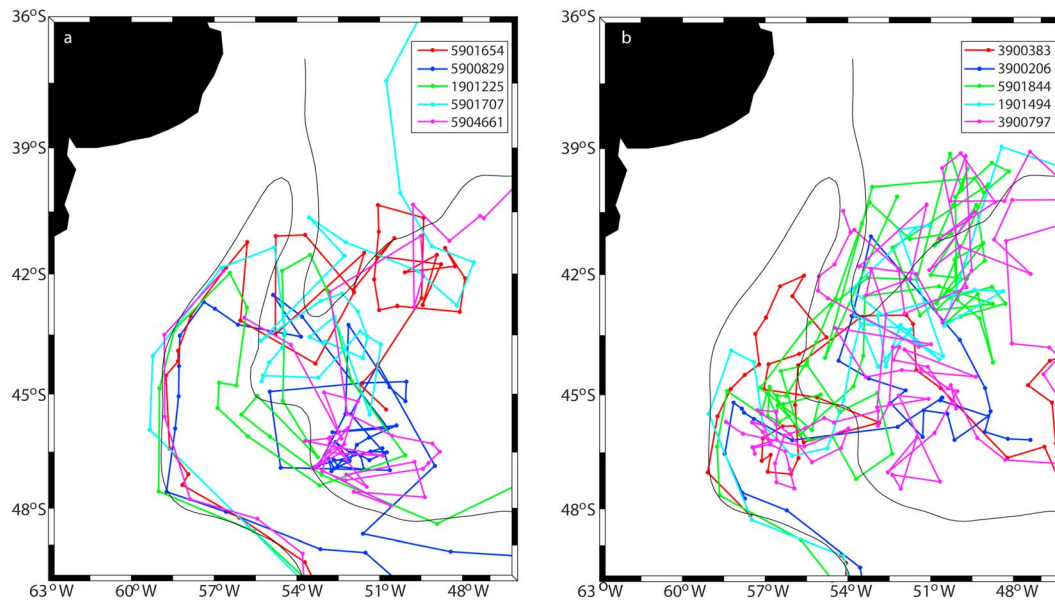


Figure 14. Selected trajectories of Argo floats (parking depth at 1,000 m) that departed the along-slope MC (a) near 42°S and (b) south of 44°S. The dots indicate the location of the float as it surfaced approximately every 10 days.

and the other half following a meridional pathway near 46°S. It seems likely that these pathways may become reinforced at times of weak along-slope MC conditions at 41°S. Under these circumstances, we could envision that the entire along-slope MC could be diverted at a southern latitude and continue as an interior northward current into the BMC near 53°W. However, based on the analysis of ADT along-slope data, Artana et al. (2016) have shown that this southern transport will not differ substantially from the values at 41°S. Hence, we may anticipate that the southern contribution will occasionally reach at least 44 Sv (mean plus SD transport at 41°S). This value, although relatively large, remains much less than our estimate of a minimum interior transport of 78.9 Sv into the BMC so we must turn to alternative water sources.

The origin of the intense interior northward flow may be connected to the outflow transport associated with the BCF. Considering only the upper 400 m, this along-front jet intensifies largely from the frontal to the confluence perimeters through the incorporation of the subantarctic waters drawn by the cyclonic SE-C. As a consequence, there is an intense along-front eastward transport cross the confluence perimeter: down to $\gamma^n = 27.81 \text{ kg/m}^3$ this amounts to $109.7 \pm 15.1 \text{ Sv}$, with about half (50.8 Sv) in baroclinic balance and the other half (58.9 Sv) associated with the flow at the reference isoneutral.

Our estimate for the along-front transport through the confluence perimeter is quite large, about twice the value of the SAC as obtained by other authors (Jullion et al., 2010; Maamaatuaiahutapu et al., 1998). The mean March 2015 ADT distribution indeed suggests that, after overtaking the perimeter of the confluence region, only a fraction of the flow will continue east as the true SAC, with most of it recirculating south to close the SE-C. We may use Jullion et al.'s (2010) transport estimates along the BCF at 35°W, $44 \pm 14 \text{ Sv}$, in order to assess the size of this eastern recirculation. Their minimum transport condition (mean minus one standard deviation, i.e., 30 Sv) would imply that the entire eastward flow along the BCF at 35°W was composed by waters of subtropical origin (recall our estimate for the BC is $29.1 \pm 8.3 \text{ Sv}$). This situation (110 Sv flowing east at 51°W with 30 Sv of subtropical origin) apparently leaves 80 Sv for recirculating south between 51°W and 35°W. However, we further notice that only about half the total along-front transport exiting the confluence perimeter is in barotropic transport (58.9 Sv) while most of the interior northward transport is barotropic (76.2 Sv out of 78.9 Sv). In the absence of any clear baroclinic-barotropic flow-conversion process, this sets an upper recirculation limit of about 61.6 Sv (the barotropic 58.9 Sv of the SAC plus the baroclinic 2.7 Sv of the SE-C).

Ferrari et al.'s (2017) analysis of the modes of spatial variability in the BMC helps identify the dominant contributions to the observed flow at the time of the cruise. These authors carried out an empirical

orthogonal function (EOF) analysis of 24 years of ADT data in the BMC and found that the first mode (explaining 24% of the variance) was associated to the northward penetration of the MC while the second mode (17% of the variance) was associated to the development of a near-zonal pattern of anomalies changing sign every couple of degrees. The temporal evolution of the ADT field previous and during our cruise supports the view of such a zonal pattern along 40–42°S, between about 47°W and 57°W, corresponding to a situation of maximum positive EOF-2 values. This condition could coincide with a period of maximum positive EOF-1 values—what Ferrari et al. (2017) identify as a strong Malvinas regime—hence leading to a short weakening of the along-slope MC (Paniagua et al., 2018) and the reinforcement of all interior recirculations, including the cyclone and anticyclone southeastern features responsible for the 78.9-Sv northward recirculation.

It is worth pointing at a possible connection between the reinforcement of the southeastern interior recirculation with the formation of anticyclonic features on the outer edge of the Zapiola Gyre (Saraceno & Provost, 2012). According to these authors, the anticyclones form on time scales on the order of a few months, that is, with intermittency comparable to the periodicity that holds most of the EOF-2 energy (Ferrari et al., 2017). Hence, the interaction of this anticyclone with the eastward along-BCF flow may be the initial factor leading to the creation of a zonal pattern of alternating ADT anomalies; confirmation of this hypothesis, however, lays beyond the objective of our study.

The above considerations endorse the idea that the observed interior northward transport (at least 78.9 Sv) is related to both the offshore diversion of the along-slope MC and the recirculation of the along-front flow exiting the BMC. The relative contributions are uncertain but our analyses suggest that most of it comes from the barotropic recirculation of the along-front flow (up to about 61.6 Sv), although a nonnegligible fraction (at least 17–18 Sv) comes from the MC itself, hence endorsing the idea of the existence of an interior MC branch. This branch would develop during the weak Malvinas regime (Ferrari et al., 2017), being associated with the upstream diversion of the along-slope MC and the intensification of near-barotropic interior mesoscale features, hence being neither a permanent nor a transient feature.

6.3. Transformation and Incorporation of Subantarctic Waters to the Subtropical Gyre

The BMC has been reported to be a key site for the incorporation of intermediate waters of southern origin (SAMW and AAIW) into the subtropical South Atlantic Ocean (Gordon, 1981; Sloyan & Rintoul, 2001). These waters subduct at the SAF and BCF to become intermediate waters, which follow north into the Atlantic Ocean in order to balance the southward flow of North Atlantic Deep Water (Garzoli & Matano, 2011; Sloyan & Rintoul, 2001).

The inverse model shows that most waters of southern origin reaching the BMC (96.8 Sv out of 166.5 Sv) belong to the intermediate strata, composed by AAIW and SAMW. Considering the waters of southern and northern origin as being separated by the BCF, we find that these intermediate waters are the ones that have the largest transport imbalances (Table 4). Indeed, the deepest layers of the confluence model experience a net gain (there is a net inflow of 11.9 Sv of AAIW and UCDW in the southern segment and a net outflow of 6.5 Sv in the northern segment) while the SAMW experiences a net loss in both segments (3.2 Sv through the south and 1.0 Sv through the north); further, the surface and subtropical waters show a net loss (net inflow of 1.8 Sv of surface and STMW through the northern segment and net outflow of 3.3 Sv through the southern segment). All together, these results reveal 5–6 Sv of net upward diapycnal transfer in the frontal system, from the intermediate to the mode and central waters.

The results in Table 4 show that most of the SAMW and AAIW transported east along the BCF are of subantarctic origin (relatively cold, fresh, and highly oxygenated) but also indicate that about 20% of these water masses come from the BC, after having traveled through the subtropical gyre (Figure 13; Garzoli & Gordon, 1996; Boebel et al., 1999; Garzoli and Matano, 2001). Valla et al. (2018) have recently argued that this recirculation of SAMW and AAIW is meridionally elongated, with the northward flow occurring only 400–600 km from the slope. Indeed, along the confluence perimeter, the isoneutral strata holding the SAMW and AAIW (26.8–27.55 kg/m³) present waters relatively fresh and with high DO values in the southern segment that contrast with saltier and much less oxygenated waters incorporated through the north (Figures 6d and 15).

Table 4
Mass Transports South and North of the BCF (in Sv; Positive Out of the Box) in the Confluence Model

Water Mass	South BCF			North BCF		
	In	Out	Net	In	Out	Net
Surface	-9.0	11.5	2.5 ± 0.4	-11.4	9.9	-1.5 ± 1.8
STMW	-16.7	17.5	0.8 ± 1.3	-14.0	13.7	-0.3 ± 2.3
SAMW	-29.1	32.3	3.2 ± 1.4	-7.3	8.3	1.0 ± 2.3
AAIW	-67.7	61.2	-6.5 ± 2.0	-6.7	9.9	3.2 ± 2.8
UCDW	-43.9	38.5	-5.4 ± 1.3	-1.3	4.6	3.3 ± 2.6
Total	-166.5	161.1	-5.4 ± 6.2	-40.6	46.2	5.4 ± 6.2

The θ , S , and DO distributions point at the existence of substantial variability in the frontal region but the details are not clear. Hence, we turn to property-property diagrams to further investigate the mixing of southern and northern waters in the frontal region (Figure 16). We consider four different groups of stations: station 3 to characterize the upstream MC, station 26 to typify the upstream BC, a third group of 20 stations within the frontal area, and a fourth group of seven stations along the confluence perimeter (stations 16 to 22); all stations (except number 3) are located north of the BCF in order to investigate the intrusions of subantarctic waters (Figure 3b).

Possibly the most evident aspect in the property-property diagrams is the practical absence of the STMW strata in the southern stations. North of the BCF, this water mass is less oxygenated in the upper slope (stations 27 and 28; not shown) and within the frontal stations; in contrast, the middle-slope BC station (26) and all stations along the confluence perimeter show STMW with relatively high DO values. This is consistent

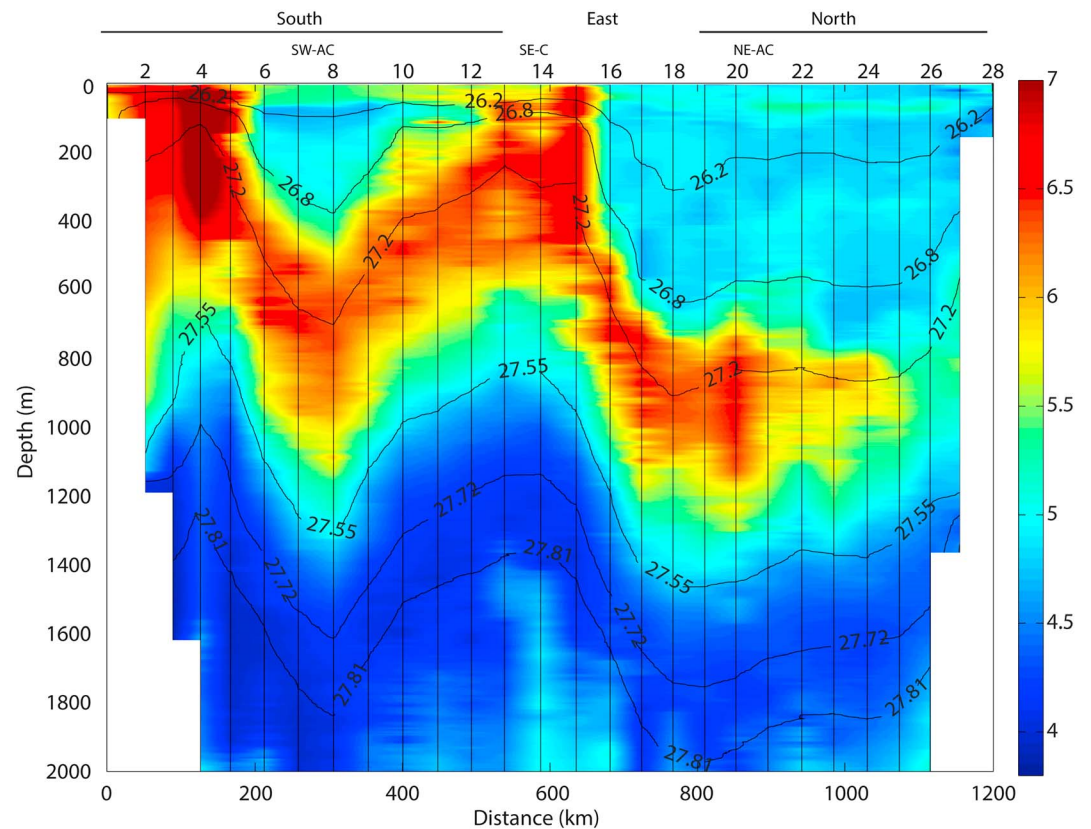


Figure 15. Vertical section of DO (mL/L) along the rim of the confluence model. The black lines represent the isoneutral water-mass boundaries used in the inverse model and the vertical black lines indicate the data points. The southern, eastern, and northern edges follow those sectors shown in Figure 1b, and the approximate extent of the mesoscale eddies is indicated.

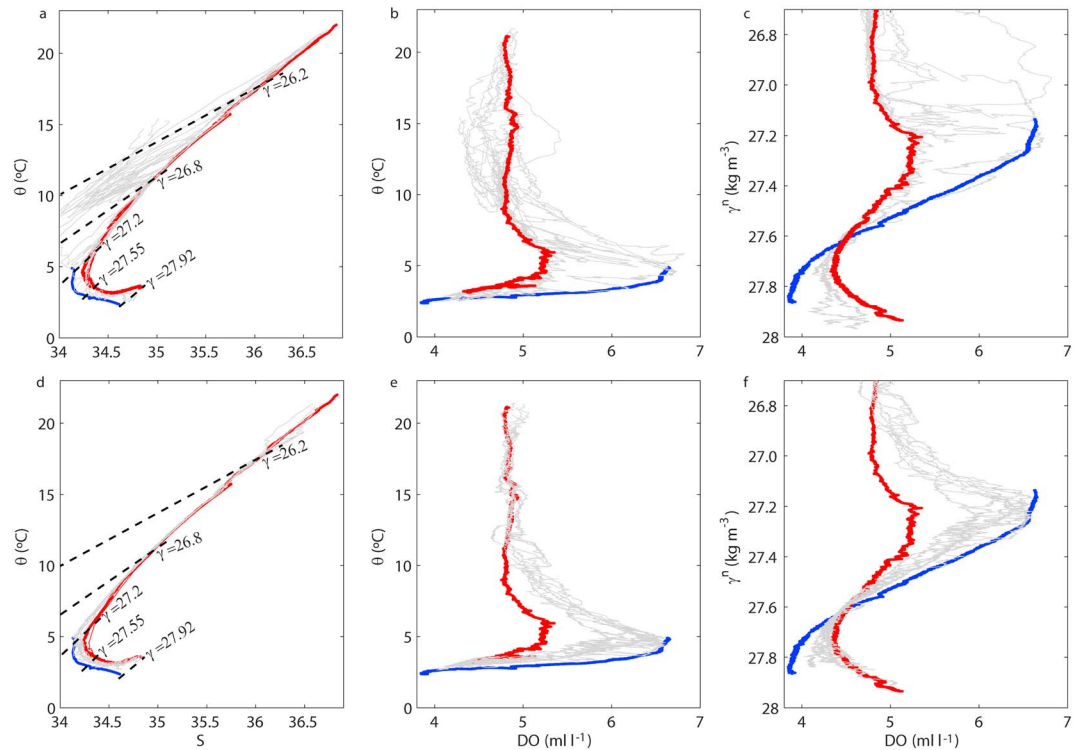


Figure 16. (a and d) θ -S diagrams, (b and e) θ -DO diagrams, and (c and f) DO as a function of γ^n . In all panels the blue and red lines characterize the MC (station 3) and BC (station 26), respectively. In the top panels the gray lines represent all stations within the frontal area and north of the BCF; in the bottom panels the gray lines correspond to stations in the eastern sector of the confluence perimeter and north of the BCF (stations 16 to 22). The black dashed lines in (a) and (d) represent the γ^n contours used to define the different water masses.

with the view that old STMW enters de BMC through the boundary current and follows along the BCF, where it mixes with younger water and becomes oxygenated, before continuing both eastward and northward (Valla et al., 2018).

Considering the intermediate waters (SAMW and AAIW), all slope southern and northern stations (here illustrated by stations 3 and 26) have similar vertical distributions of θ , S, and DO (Figure 16). In contrast, within the frontal stations there is high variability between adjacent stations and depths due to substantial horizontal interleaving. Similarly to what happened with the STMW, the variability in these deep strata is largely gone by the time these waters reach the confluence perimeter.

We may investigate what processes are behind this smoothing out of properties by considering the case of along-isopycnal mixing between two end-members. Specifically, we select stations 3 and 26 to, respectively, characterize the MC and BC conditions and, for each neutral density level, we obtain the corresponding temperature, salinity, and DO end-water values. The temperature, salinity, and DO values of a water parcel at any neutral-density level of a frontal station are then expressed as the linear combination of the two end-water types. For steady state conditions and conservative water properties, along-isopycnal mixing should lead to the same mixing fraction for all water properties, so that any observed difference may be attributed to diapycnal mixing.

The results of the above procedure are shown in Figure 17, with the θ , S, and DO profiles plotted as a function of γ^n . In the conservative-temperature versus neutral-density profile we show the fraction of the BC water type that contributes to the observed value (the complement to one represents the fraction of the MC water type); notice that the contribution of the BC and MC water types to the observed temperature is inversely proportional to the along-isopycnal difference between the observed temperature and the BC and MC temperatures, respectively. If we repeat the procedure for the salinity and DO profiles we would obtain water fractions that, for entirely along-isopycnal mixing, should not change (given the smallness of

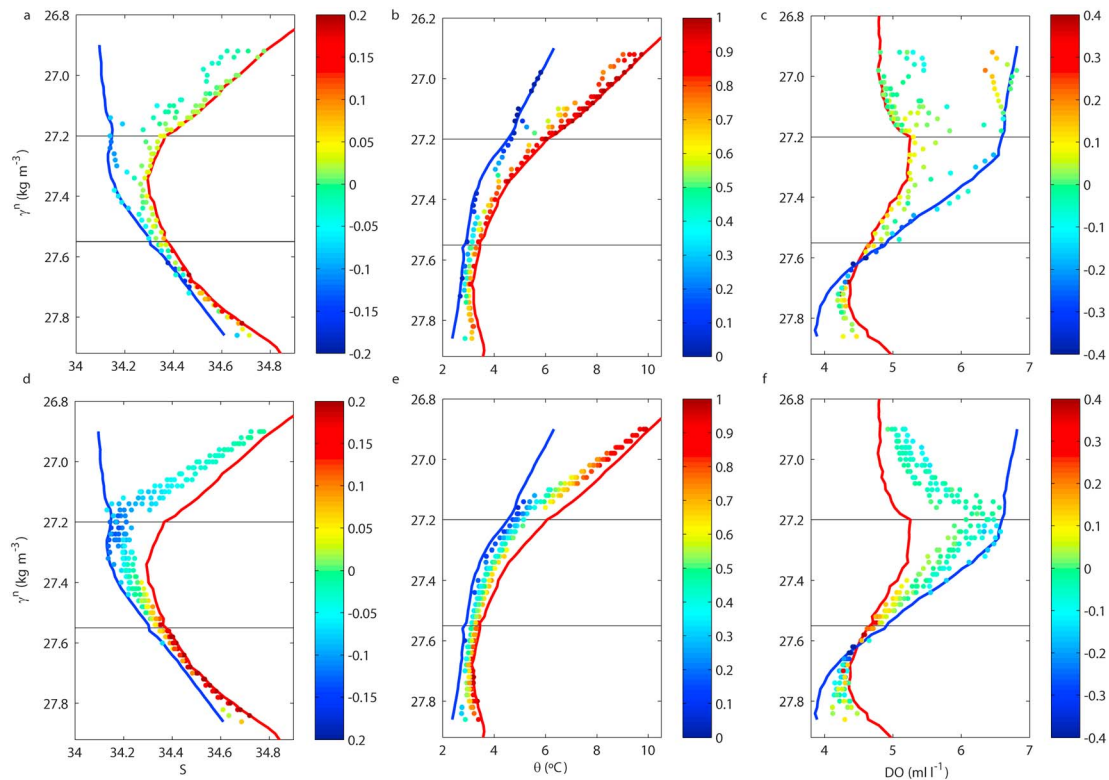


Figure 17. (a and d) S , (b and e) θ , and (c and f) DO as a function of γ^{ρ} , at intervals of 0.02 kg/m^3 . In all panels the blue and red lines characterize the MC (station 3) and BC (station 26), respectively, and the horizontal lines delimit the different water masses. In the top panels, the dots represent data from stations north of the BCF within the frontal area; in the bottom panels, the dots correspond to stations in the eastern sector of the confluence perimeter and north of the BCF (stations 16 to 22). (b and e) The color-coded values indicate the mixing fraction, with zero indicating pure MC water (dark blue) and one denoting pure BC water (dark red); (a and d) difference between the S and θ mixing fractions, and (c and f) difference between the DO and θ mixing fractions (notice the change in color code).

the frontal and confluence domains, we may reasonably assume DO as conservative). However, we observe that the S and θ mixing fractions differ by up to 20%, and the DO and θ mixing fractions differ by as much as 40%. We interpret these differences as the consequence of diapycnal mixing between water masses that bear different ratios among water properties. For example, over the entire SAMW stratum DO is approximately constant but both θ and S change linearly with depth, so that vertical mixing brings larger property anomalies for θ and S than for DO .

7. Concluding Remarks

The Brazil-Malvinas Confluence (BMC) is a very intense frontal system that results from the encountering of two major western boundary currents: the northward Malvinas Current (MC), which carries subantarctic waters, and the southward Brazil Current (BC), which carries a mixture of subantarctic and subtropical waters. At the BMC, the surface manifestation of this frontal system is the Brazil Current Front (BCF), set at the absolute dynamic topography (ADT) contour of 0.30 m (Ferrari et al., 2017).

The MC is possibly the strongest equatorward boundary current in the entire global ocean, with intense surface and subsurface currents. As the MC encounters the BC along the continental slope, it undergoes a sharp 180° turn and the entire frontal system follows south, in what is known as the MC retroflexion (MRC) and BC overshoot (BCO). The characteristics of this convoluted turn and its leeward structure at 41°S has been the subject of several recent studies (Artana et al., 2018; Ferrari et al., 2017; Paniagua et al., 2018; Valla et al., 2018). These studies show that the BMC has substantial temporal variability, between times of an intense impinging MC and a powerful MRC-BCO return flow, and times when the MC weakens, characterized by the MRC-BCO breaking into an isolated anticyclone and a cyclone forming further east.

Our study of this intense frontal system refers to the March 2015 conditions, as observed with cruise data (8–22 March) encircling the BMC at two different spatial scales. These data are analyzed with an inverse model, helped by both altimetry data and velocity time series over the slope near 41°S, in order to assess the patterns of circulation associated with the boundary and frontal currents, their barotropic and baroclinic contributions, and the intensity of the cross-frontal exchange in the upper 2,000 m. The model reference level is set at $\gamma^n = 27.81 \text{ kg/m}^3$ (found between 1,400 and 2,000 m) for the outer (confluence) region and at $z = 400 \text{ m}$ for the inner (frontal) area, and altimetry data are used to connect both domains.

The March 2015 BC depicts a fairly classic picture: its along-slope transport down to $\gamma^n = 27.81 \text{ kg/m}^3$ ($29.1 \pm 8.3 \text{ Sv}$) lies in the middle of the reported range of variation, largely baroclinic (29.0 Sv). Most of the flow belongs to the surface and Subtropical Mode Waters ($18.0 \pm 2.0 \text{ Sv}$), although there is a quite significant southward flow of subantarctic waters ($10.2 \pm 2.8 \text{ Sv}$). These southward flowing subantarctic waters are much depleted in oxygen, indicating that they have followed a long subtropical pathway before returning to the northern edge of the BMC.

The situation for the MC and the eastward jet associated with the BCF, however differs greatly from the classic description. The ADT reveals conditions that characterize a weak along-slope MC at 41°S: the northward loop is strangulated and the MRC-BCO system has evolved into an anticyclone, and an elongated cyclone is formed further east. Surprisingly, this corresponds to a period (January–April) that Ferrari et al. (2017) and Paniagua et al. (2018) identify as a strong Malvinas regime. Close inspection of Paniagua's time series, however, shows that the along-slope MC at 41°S weakened substantially during the first 10 days of March, precisely before our cruise. Our inverse model indeed shows a weak along-slope MC near the collision latitude (39.5°S) at the beginning of the cruise and, in contrast, finds a remarkably intense northward interior flow, located between the eastern anticyclone and cyclone (near 53°W). Down to $\gamma^n = 27.81 \text{ kg/m}^3$, the along-slope MC transports $28.3 \pm 1.4 \text{ Sv}$, the anticyclone recirculates up to $59.3 \pm 10.7 \text{ Sv}$, and the interior flow accounts for at least $78.9 \pm 13.7 \text{ Sv}$.

We have carefully explored the origin of the intense interior northward flow. The temporal evolution of the sea-surface ADT and the trajectories of Argo floats suggest that there is an eastward diversion of the along-slope upstream MC at latitudes 42°S or greater, potentially favoring the interior branch. Periods of weak along-slope MC transport probably come together with the intensification of the interior currents, as the convoluted MC and MRC strangle, and the slope flow is deviated at either 42°S or 46°S. During this weak-MC periods, it seems possible that the upstream (beyond 46°S) along-slope MC flow finds an alternative interior pathway to reach the BCF. However, the interior northward current is also sustained by the cyclonic recirculation of the water outflow along the BCF. Indeed, we observe a very intense ($109.7 \pm 15.1 \text{ Sv}$) South Atlantic Current (SAC) exiting the convergence zone along the BCF and the ADT field and barotropic-baroclinic decomposition suggest that a major fraction of this outflow recirculates cyclonically to feed the interior flow. Grossly speaking, we estimate that the offshore diversion of no less than 17–18 Sv from the upstream along-slope MC and the cyclonic recirculation of some 60 Sv of along-front outflow add together to produce the observed interior northward transport; further, we anticipate that similar situations may occur during the occurrence of a weak-Malvinas regime, hence leading to the notion of an intermittent interior MC.

The inverse model provides other pieces of useful information. The first one is a large barotropic contribution in the MC and SAC for water layers lighter than $\gamma^n = 27.81 \text{ kg/m}^3$, by barotropic meaning the contribution associated with the velocities at that reference level. Over half of the SAC transport responds to the reference velocities (58.9 Sv) and the rest to the baroclinic velocities (50.8 Sv). Regarding the along-slope MC at 41°S, 13.3 Sv are baroclinic and 15.0 Sv are barotropic; for the interior northward flow, nearly the entire flow is barotropic (76.2 out of 78.9 Sv). Further, about 70% of this southern inflow corresponds to Subantarctic Mode and Intermediate Waters (SAMW and AAIW, respectively).

Another relevant piece of information is the net exchange of subantarctic and subtropical waters through the BMC, along some 500 km of the frontal system. The water balance per stratum reveals about 5–6 Sv of net upward diapycnal transfer in the confluence region, with intermediate AAIW and SAMW being transferred to the shallower layers. In particular, we find a substantial net inflow (11.9 Sv) of AAIW and Upper Circumpolar Deep Waters (UCDW) south of the BCF. Assuming along-isopycnal mixing, we calculate the mixing fractions for different water properties, which reveal large differences depending on water

property: up to 20% between temperature and salinity and 40% between temperature and dissolved oxygen. Both evidences—the transport imbalances per layer on both sides of the BCF and the differences in mixing fraction from one property to another—point at substantial cross-frontal and diapycnal water exchange in the BMC.

The BMC, at the crossroads of subantarctic and subtropical waters, is a regional process with global implications. We are urged to improve our understanding of its different modes of functioning, characterized by extraordinary temporal and spatial variability (e.g., Artana et al., 2018; Ferrari et al., 2017; Paniagua et al., 2018; Valla et al., 2018). Our results show that the regional pattern of circulation evolves on time scales on the order of weeks and emphasizes the idea that any description of the BMC cannot be understood without monitoring the time history of the upstream along-slope (BC and MC) and interior (Zapiola gyre) conditions. The time series of satellite ADT and mooring velocity indeed expose the existence of many possible combinations, resembling a baroque musical improvisation with an unpredictable outcome. Additionally, there are short and fast submesoscale processes that produce noticeable water mass transformations in the frontal system, causing an even more capricious evolution. The challenge is to decipher the spatial and temporal predominant rhythms but also the way they preferentially connect to create a perpetually changing melody.

Acknowledgments

We are very grateful to the crew, technicians, and scientists in the R/V *Hespérides* for their work during TIC-MOC cruise. We are also indebted to Fabrice Hernandez and the entire MyOcean team at Mercator Ocean for providing the one-week-window daily forecasts during the TIC-MOC cruise. We are also thankful to Silvia Garzoli and another two anonymous reviewers for their constructive and useful comments and suggestions. This research has been supported by the Spanish Government through projects TIC-MOC (CTM2011-28867) and VA-DE-RETRO (CTM2014-56987-P), and by RIS-3, PO Feder Canarias through project BOUNDARY (ProID2017010083). Dorleta Orúe-Echevarría has been funded through an FPU contract (ref. FPU2013-02884). In situ CTD and ADCP data are available at Pelegrí et al. (2018). Satellite altimetry data are available at Copernicus Marine Environment monitoring service (CMEMS; <http://marine.copernicus.eu/>) and SST data at NOAA AVHRR Pathfinder version 5.3 (<https://data.nodc.noaa.gov>). Data for the determination of climatological isoneutral surfaces are available at NOAA's National Centers for Environmental Information World Ocean Database 2013 (<https://www.nodc.noaa.gov/OC5/WOD13/>). Argo data were collected and made freely available by the International Argo Program and the national programs that contribute to it (<http://www.argo.ucsd.edu/> and <http://www.jcommops.org>). The Argo Program is part of the Global Ocean Observing System (<http://doi.org/10.17882/42182>). This article is a publication of the Unidad Océano y Clima de la Universidad de Las Palmas de Gran Canaria, a R&D&I CSIC-associate unit.

References

- Artana, C., Ferrari, R., Koenig, Z., Saraceno, M., Piola, A. R., & Provost, C. (2016). Malvinas current variability from Argo floats and satellite altimetry. *Journal of Geophysical Research: Oceans*, *121*, 4854–4872. <https://doi.org/10.1002/2016JC011889>
- Artana, C., Ferrari, R., Koenig, Z., Sennéchaël, N., Saraceno, M., Piola, A. R., & Provost, C. (2018). Malvinas current volume transport at 41°S: A 24 yearlong time series consistent with mooring data from 3 decades and satellite altimetry. *Journal of Geophysical Research: Oceans*, *123*, 378–398. <https://doi.org/10.1002/2017JC013600>
- Barré, N., Provost, C., Renault, A., & Sennéchaël, N. (2011). Fronts, meanders and eddies in Drake Passage during the ANT-XXIII/3 cruise in January–February 2006: A satellite perspective. *Deep Sea Research, Part II*, *58*(25–26), 2533–2554. <https://doi.org/10.1016/j.dsr2.2011.01.003>
- Boebel, O., Schmid, C., & Zenk, W. (1999). Kinematic elements of Antarctic intermediate water in the western South Atlantic. *Deep-Sea Research Part II: Topical Studies in Oceanography*, *46*(1–2), 355–392. [https://doi.org/10.1016/S0967-0645\(98\)00104-0](https://doi.org/10.1016/S0967-0645(98)00104-0)
- Ferrari, R., Artana, C., Saraceno, M., Piola, A. R., & Provost, C. (2017). Satellite altimetry and current-meter velocities in the Malvinas Current at 41°S: Comparisons and modes of variations. *Journal of Geophysical Research: Oceans*, *122*, 9572–9590. <https://doi.org/10.1002/2017JC013340>
- Ganachaud, A. (2003a). Error budget of inverse box models: The North Atlantic. *Journal of Atmospheric and Oceanic Technology*, *20*(11), 1641–1655. [https://doi.org/10.1175/1520-0426\(2003\)020<1641:EBOIBM>2.0.CO;2](https://doi.org/10.1175/1520-0426(2003)020<1641:EBOIBM>2.0.CO;2)
- Ganachaud, A. (2003b). Large-scale mass transports, water mass formation, and diffusivities estimated from World Ocean Circulation Experiment (WOCE) hydrographic data. *Journal of Geophysical Research*, *108*(C7), 3213. <https://doi.org/10.1029/2002JC001565>
- Garzoli, S. L. (1993). Geostrophic velocity and transport variability in the Brazil-Malvinas Confluence. *Deep Sea Research Part I: Oceanographic Research Papers*, *40*(7), 1379–1403. [https://doi.org/10.1016/0967-0637\(93\)90118-M](https://doi.org/10.1016/0967-0637(93)90118-M)
- Garzoli, S. L., Baringer, M. O., Dong, S., Perez, R. C., & Yao, Q. (2013). South Atlantic meridional fluxes. *Deep Sea Research Part I: Oceanographic Research Papers*, *71*(supplement C), 21–32. <https://doi.org/10.1016/j.dsr.2012.09.003>
- Garzoli, S. L., & Garraffo, Z. (1989). Transports, frontal motions and eddies at the Brazil-Malvinas currents confluence. *Deep Sea Research Part A: Oceanographic Research Papers*, *36*, 681–703. [https://doi.org/10.1016/01980149\(89\)90145-3](https://doi.org/10.1016/01980149(89)90145-3)
- Garzoli, S. L., & Gordon, A. L. (1996). Origins and variability of the Benguela current. *Journal of Geophysical Research*, *101*(C1), 897–906. <https://doi.org/10.1029/95JC03221>
- Garzoli, S. L., & Matano, R. (2011). The South Atlantic and the Atlantic meridional overturning circulation. *Deep Sea Research Part II: Topical Studies in Oceanography*, *94*(C8), 10,817–11,847. <https://doi.org/10.1029/JC094iC08p10817>
- Goni, G., Kamholz, S., Garzoli, S., & Olson, D. (1996). Dynamics of the Brazil-Malvinas Confluence based on inverted echo sounders and altimetry. *Journal of Geophysical Research*, *101*(C7), 16,273–16,289. <https://doi.org/10.1029/96JC01146>
- Goni, G. J., Bringas, F., & DiNezio, P. N. (2011). Observed low frequency variability of the Brazil current front. *Journal of Geophysical Research*, *116*, C10037. <https://doi.org/10.1029/2011JC007198>
- Goni, G. J., & Wainer, I. (2001). Investigation of the Brazil current front variability from altimeter data. *Journal of Geophysical Research*, *106*(C12), 31,117–31,128. <https://doi.org/10.1029/2000JC000396>
- Goniadzi, D., Borús, J., Almeida, G., Díaz, L., Núñez, V., & Contreras, G. (2015). Posibles escenarios hidrológicos en la Cuenca del Plata durante el periodo Abril-Mayo-Junio 2015. Instituto Nacional del Agua.
- Gordon, A. L. (1981). South Atlantic thermocline ventilation. *Deep Sea Research Part A: Oceanographic Research Papers*, *28*(11), 1239–1264. [https://doi.org/10.1016/0198-0149\(81\)90033-9](https://doi.org/10.1016/0198-0149(81)90033-9)
- Gordon, A. L., & Greengrove, C. L. (1986). Geostrophic circulation of the Brazil-Falkland confluence. *Deep Sea Research Part A: Oceanographic Research Papers*, *33*(5), 573–585. [https://doi.org/10.1016/0198-0149\(86\)90054-3](https://doi.org/10.1016/0198-0149(86)90054-3)
- Jullion, L., Heywood, K. J., Naveira Garabato, A. C., & Stevens, D. P. (2010). Circulation and water mass modification in the Brazil–Malvinas confluence. *Journal of Physical Oceanography*, *40*(5), 845–864. <https://doi.org/10.1175/2009jp04174.1>
- King, B. A., Firing, E., & Joyce, T. M. (2001). Shipboard observations during WOCE. In G. Siedler, J. Church, & J. Gould (Eds.), *Ocean Circulation and Climate: Observing and Modelling the Global Ocean* (pp. 99–122). San Diego, CA: Academic Press. [https://doi.org/10.1016/S0074-6142\(01\)80114-5](https://doi.org/10.1016/S0074-6142(01)80114-5)
- Lee, S. K., Pelegrí, J. L., & Kroll, J. (2001). Slope control in Western boundary currents. *Journal of Physical Oceanography*, *31*(11), 3349–3360. [https://doi.org/10.1175/1520-0485\(2001\)031<3349:Sciwbcb>2.0.Co;2](https://doi.org/10.1175/1520-0485(2001)031<3349:Sciwbcb>2.0.Co;2)

- Legeckis, R., & Gordon, A. L. (1982). Satellite observations of the Brazil and Falkland currents—1975–1976 and 1978. *Deep Sea Research Part A. Oceanographic Research Papers*, 29(3), 375–401. [https://doi.org/10.1016/0198-0149\(82\)90101-7](https://doi.org/10.1016/0198-0149(82)90101-7)
- Lentini, C. A. D., Goni, G. J., & Olson, D. B. (2006). Investigation of Brazil current rings in the confluence region. *Journal of Geophysical Research*, 111, L18605. <https://doi.org/10.1029/2005JC002988>
- Maamaatuaiahutapu, K., Garçon, V., Provost, C., Boulahdid, M., & Osiroff, A. P. (1992). Brazil-Malvinas Confluence: Water mass composition. *Journal of Geophysical Research*, 97(C6), 9493–9505. <https://doi.org/10.1029/92JC00484>
- Maamaatuaiahutapu, K., Garçon, V., Provost, C., & Mercier, H. (1998). Transports of the Brazil and Malvinas currents at their confluence. *Journal of Marine Research*, 56, 417–438. <https://doi.org/10.1357/002224098321822366>
- Mason, E., Pascual, A., Gaube, P., Ruiz, S., Pelegrí, J. L., & Delepouille, A. (2017). Subregional characterization of mesoscale eddies across the Brazil-Malvinas Confluence. *Journal of Geophysical Research: Oceans*, 122, 3329–3357. <https://doi.org/10.1002/2016JC012611>
- Matano, R. P., Palma, E. D., & Piola, A. R. (2010). The influence of the Brazil and Malvinas currents on the southwestern Atlantic shelf circulation. *Ocean Science Discussions*, 6(4), 983–995. <https://doi.org/10.5194/os-6-983-2010>
- McIntosh, P. C., & Rintoul, S. R. (1997). Do box inverse models work? *Journal of Physical Oceanography*, 27(2), 291–308. [https://doi.org/10.1175/1520-0485\(1997\)027<0291:dbimw>2.0.co;2](https://doi.org/10.1175/1520-0485(1997)027<0291:dbimw>2.0.co;2)
- Olson, D. B., Podestá, G. P., Evans, R. H., & Brown, O. B. (1988). Temporal variations in the separation of Brazil and Malvinas currents. *Deep Sea Research Part A. Oceanographic Research Papers*, 35(12), 1971–1990. [https://doi.org/10.1016/0198-0149\(88\)90120-3](https://doi.org/10.1016/0198-0149(88)90120-3)
- Orsi, A. H., Whitworth, T., & Nowlin, W. D. (1995). On the meridional extent and fronts of the Antarctic circumpolar current. *Deep Sea Research Part I: Oceanographic Research Papers*, 42(5), 641–673. [https://doi.org/10.1016/0967-0637\(95\)00021-W](https://doi.org/10.1016/0967-0637(95)00021-W)
- Orúe-Echevarría, D., Pelegrí, J. L., Alonso-González, I. J., Benítez-Barrios, V. M., De La Fuente, P., Emelianov, M., et al. (2019). Dataset on the TIC-MOC cruise onboard the R/V *Hespérides*, March 2015, Brazil-Malvinas Confluence. *Data in Brief*, 22, 185–194. <https://doi.org/10.1016/j.dib.2018.12.004>
- Ott, M. W. (2002). An improvement in the calculation of ADCP velocities. *Journal of Atmospheric and Oceanic Technology*, 19(10), 1738–1741. [https://doi.org/10.1175/1520-0426\(2002\)019<1738:Aaitco>2.0.Co;2](https://doi.org/10.1175/1520-0426(2002)019<1738:Aaitco>2.0.Co;2)
- Paniagua, G. F., Saraceno, M., Piola, A. R., Guerrero, R., Provost, C., Ferrari, R., et al. (2018). Malvinas current at 40°–41°S: First assessment of temperature and salinity temporal variability. *Journal of Geophysical Research: Oceans*, 123(8), 5323–5340. <https://doi.org/10.1029/2017JC013666>
- Pascual, A., Bouffard, J., Ruiz, S., Buongiorno Nardelli, B., Vidal-Vijande, E., Escudier, R., et al. (2013). Recent improvements in mesoscale characterization of the western Mediterranean Sea: Synergy between satellite altimetry and other observational approaches. *Scientia Marina*, 77(1), 19–36. <https://doi.org/10.3989/scimar.03740.15A>
- Pelegrí, J. L., Orúe-Echevarría, D., Alonso-González, I. J., Benítez-Barrios, V. M., De La Fuente, P., Emelianov, M., et al. (2018). Data for the March 2015 TIC-MOC cruise, R/V *Hespérides*, Brazil-Malvinas Confluence. Mendeley data, v2. [DOI:10.17632/hk8t43z3t3.2](https://doi.org/10.17632/hk8t43z3t3.2)
- Peterson, R. G. (1992). The boundary currents in the western Argentine basin. *Deep Sea Research Part A. Oceanographic Research Papers*, 39(3–4), 623–644. [https://doi.org/10.1016/0198-0149\(92\)90092-8](https://doi.org/10.1016/0198-0149(92)90092-8)
- Peterson, R. G., & Whitworth, T. (1989). The subantarctic and polar fronts in relation to deep water masses through the southwestern Atlantic. *Journal of Geophysical Research*, 94(C8), 10,817–10,838. <https://doi.org/10.1029/JC094iC08p10817>
- Piola, A., & Matano, R. (2001). The South Atlantic Western boundary currents Brazil/Falkland (Malvinas) currents. In J. M. Steel, S. A. Thorpe, & K. K. Turekin (Eds.), *Encyclopedia of Ocean Sciences* (pp. 340–349). Waltham, MA: Academic Press. <https://doi.org/10.1006/rvos.2001.0358>
- Piola, A. R., Franco, B. C., Palma, E. D., & Saraceno, M. (2013). Multiple jets in the Malvinas current. *Journal of Geophysical Research: Oceans*, 118, 2107–2117. <https://doi.org/10.1002/jgrc.20170>
- Polzin, K., Kunze, E., Hummon, J., & Firing, E. (2002). The finescale response of lowered ADCP velocity profiles. *Journal of Atmospheric and Oceanic Technology*, 19(2), 205–224. [https://doi.org/10.1175/1520-0426\(2002\)019<0205:TFROLA>2.0.CO;2](https://doi.org/10.1175/1520-0426(2002)019<0205:TFROLA>2.0.CO;2)
- Provost, C., Escoffier, C., Maamaatuaiahutapu, K., Kartavtseff, A., & Garçon, V. (1999). Subtropical mode waters in the South Atlantic Ocean. *Journal of Geophysical Research*, 104(C9), 21,033–21,049. <https://doi.org/10.1029/1999JC000049>
- Pujol, M.-I., Faugère, Y., Taburet, G., Dupuy, S., Pelloquin, C., Ablain, M., & Picot, N. (2016). DUACS DT2014: The new multi-mission altimeter data set reprocessed over 20 years. *Ocean Science*, 12(5), 1067–1090. <https://doi.org/10.5194/os-12-1067-2016>
- Saraceno, M., Guerrero, R., Piola, A. R., Provost, C., Perault, F., Ferrari, R., et al. (2017). Malvinas current 2014–2015: Mooring velocities. SEANO. <https://doi.org/10.17882/51492>
- Saraceno, M., & Provost, C. (2012). On eddy polarity distribution in the southwestern Atlantic. *Deep Sea Research Part I*, 69, 62–69. <https://doi.org/10.1016/j.dsr.2012.07.005>
- Saraceno, M., Provost, C., Piola, A. R., Bava, J., & Gagliardini, A. (2004). Brazil Malvinas frontal system as seen from 9 years of advanced very high resolution radiometer data. *Journal of Geophysical Research*, 109, C05027. <https://doi.org/10.1029/2003JC002127>
- Sato, O. T., & Polito, P. S. (2014). Observation of South Atlantic subtropical mode waters with Argo profiling float data. *Journal of Geophysical Research: Oceans*, 119, 2860–2881. <https://doi.org/10.1002/2013JC009438>
- Saunders, P. M., & King, B. A. (1995). Bottom currents derived from a shipborne ADCP on WOCE cruise A11 in the South Atlantic. *Journal of Physical Oceanography*, 25(3), 329–347. [https://doi.org/10.1175/1520-0485\(1995\)025<0329:Bocfas>2.0.co;2](https://doi.org/10.1175/1520-0485(1995)025<0329:Bocfas>2.0.co;2)
- Schmid, C. (2014). Mean vertical and horizontal structure of the subtropical circulation in the South Atlantic from three-dimensional observed velocity fields. *Deep Sea Research Part I: Oceanographic Research Papers*, 91(supplement C), 50–71. <https://doi.org/10.1016/j.dsr.2014.04.015>
- Sloyan, B. M., & Rintoul, S. R. (2001). Circulation, renewal, and modification of Antarctic mode and intermediate water. *Journal of Physical Oceanography*, 31(4), 1005–1030. [https://doi.org/10.1175/1520-0485\(2001\)031<1005:cramoa>2.0.co;2](https://doi.org/10.1175/1520-0485(2001)031<1005:cramoa>2.0.co;2)
- Spadone, A., & Provost, C. (2009). Variations in the Malvinas current volume transport since October 1992. *Journal of Geophysical Research*, 114, C02002. <https://doi.org/10.1029/2008JC004882>
- Stramma, L. (1989). The Brazil current transport south of 23°S. *Deep Sea Research Part A. Oceanographic Research Papers*, 36(4), 639–646. [https://doi.org/10.1016/0198-0149\(89\)90012-5](https://doi.org/10.1016/0198-0149(89)90012-5)
- Stramma, L., & Peterson, R. G. (1990). The South Atlantic current. *Journal of Physical Oceanography*, 20(6), 846–859. [https://doi.org/10.1175/1520-0485\(1990\)020<0846:Tsac>2.0.Co;2](https://doi.org/10.1175/1520-0485(1990)020<0846:Tsac>2.0.Co;2)
- Thurnherr, A. M., Goszczko, L., & Bahr, F. (2017). Improving LADCP velocity with external heading, pitch, and roll. *Journal of Atmospheric and Oceanic Technology*, 34(8), 1713–1721. <https://doi.org/10.1175/jtech-d-16-0258.1>
- Valla, D., Piola, A. R., Meinen, C. S., & Campos, E. (2018). Strong mixing and recirculation in the northwestern Argentine Basin. *Journal of Geophysical Research: Oceans*, 123(7), 4624–4648. <https://doi.org/10.1029/2018JC013907>

- Vivier, F., & Provost, C. (1999a). Direct velocity measurements in the Malvinas current. *Journal of Geophysical Research*, *104*(C9), 21,083–21,103. <https://doi.org/10.1029/1999JC900163>
- Vivier, F., & Provost, C. (1999b). Volume transport of the Malvinas current: Can the flow be monitored by TOPEX/POSEIDON? *Journal of Geophysical Research*, *104*(C9), 21,105–21,122. <https://doi.org/10.1029/1999JC900056>
- Wunsch, C. (1978). The North Atlantic general circulation west of 50°W determined by inverse methods. *Reviews of Geophysics*, *16*(4), 583–620. <https://doi.org/10.1029/RG016i004p00583>
- Wunsch, C. (1996). *The Ocean Inverse Circulation Inverse Problem* (442 pp.). Cambridge, UK: Cambridge University Press. <https://doi.org/10.1017/CBO9780511629570>
- Zemba, J. C. (1991). The structure and transport of the Brazil Current between 27° and 36° south. (PhD thesis) (160 pp.). Massachusetts Institute of Technology/Woods Hole Oceanographic Institution.